



12-2003

Analysis of wind tunnel model support system vibration

Kristi D. Holland

Recommended Citation

Holland, Kristi D., "Analysis of wind tunnel model support system vibration. " Master's Thesis, University of Tennessee, 2003.
https://trace.tennessee.edu/utk_gradthes/5237

This Thesis is brought to you for free and open access by the Graduate School at Trace: Tennessee Research and Creative Exchange. It has been accepted for inclusion in Masters Theses by an authorized administrator of Trace: Tennessee Research and Creative Exchange. For more information, please contact trace@utk.edu.

To the Graduate Council:

I am submitting herewith a thesis written by Kristi D. Holland entitled "Analysis of wind tunnel model support system vibration." I have examined the final electronic copy of this thesis for form and content and recommend that it be accepted in partial fulfillment of the requirements for the degree of Master of Science, with a major in Mechanical Engineering.

Ahmad Vakili, Major Professor

We have read this thesis and recommend its acceptance:

Accepted for the Council:

Carolyn R. Hodges

Vice Provost and Dean of the Graduate School

(Original signatures are on file with official student records.)

To the Graduate Council:

I am submitting herewith a thesis written by Kristi D. Holland entitled "Analysis of Wind Tunnel Model Support System Vibration." I have examined the final paper copy of this thesis for form and content and recommend that it be accepted in partial fulfillment of the requirements for the degree of Master of Science, with a major in Mechanical Engineering.



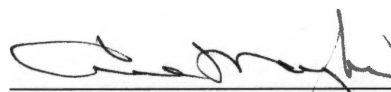
Ahmad Vakili, Major Professor

We have read this thesis and recommend its acceptance:





Acceptance for the Council:



Vice Provost and Dean of
Graduate Studies

Thesis
2003
.H64

Analysis of Wind Tunnel Model Support System Vibration

**A Thesis
Presented for the
Master of Science
Degree**

The University of Tennessee, Knoxville

**Kristi D. Holland
December 2003**

ACKNOWLEDGEMENTS

I would like to sincerely thank my advisor Dr. Ahmad Vakili for all of his guidance and support throughout my work at University of Tennessee Space Institute. I would also like to thank Arnold Engineering Development Center for supporting this research. In addition, I would like to thank Brenda Brooks for acquiring the numerous journal articles I requested, and a special thanks also goes to Russell Groff for the expertise he passed along to me about ANSYS. I truly could not have completed the finite element modeling without his help.

I would especially like to thank my husband, Nick, for his patience, encouragement, and advice while I worked on this degree and my best friend, Cassandra, for her encouragement and prayers. Most importantly, I would like to thank God for all He has done for me this past year and a half, and I give Him all the glory for my accomplishments.

ABSTRACT

A number of wind tunnel test facilities are experiencing undesirable vibrations of the model support system. These vibrations lead to a number of problems. For example, when the model vibrates, the test conditions are no longer realistic. The dynamics of the model and sting cause the flow to become unsteady. The data collected from unsteady flow differs from that collected when the flow is steady state. Another major concern is that the vibrations could cause the model to come apart and damage components inside the wind tunnel, such as compressors or blades, which could be costly to repair. Therefore, limitations are placed on the conditions at which the tunnel can be operated.

In order to reduce the vibrations in the wind tunnel, the vibration must first be measured, which will be the primary topic of this paper. The purpose of this thesis was to design a generic model support system that closely represents a typical wind tunnel model support system (sting, balance, and a generic model), measure the vibration in the model support system, perform modal analysis, and compare the results with finite element modeling. Passive damping techniques were also explored experimentally.

Several experimental methods were considered as options to measure deflection of a vibrating beam. This study utilizes a cylindrical beam as a simplification of the sting problem. Three experiments were conducted, and finite element analysis was performed on the model.

Experimental results showed that the model behaved similar to a typical wind tunnel model. They also showed that the insertion of a sleeve around the sting could be an effective way to attenuate the frequency, once improved. Finite element solutions obtained were generally in good agreement with the results from the experiments.

TABLE OF CONTENTS

I.	INTRODUCTION	1
II.	LITERATURE REVIEW AND BACKGROUND	3
	Literature Review	3
	Case Study 1	3
	Case Study 2	4
	Case Study 3	6
	Case Study 4	6
	Case Study 5	6
	Background	7
	What is modal analysis?	7
	Modal Analysis Theory	7
III.	EXPERIMENTAL APPROACH	9
	Model Design	10
	Shaker Table Experiment Without Damping	14
	Equipment List and Setup	14
	Equipment List	14
	Setup	14
	Procedure	15
	Shaker Table Experiment With Damping	16
	Equipment List and Setup	16
	Procedure	17
	Impulse Testing Experiment	17
	Equipment List and Setup	19
	Equipment List	19
	Setup	19
	Procedure	19
	Finite Element Analysis	21
	Unconstrained Condition	23
	Sting Only Configuration	23
	Sting + Nut Configuration	27
	Sting + Nut + Balance and Calibration Device Configuration	27
	Constrained Condition	27
IV.	RESULTS AND ANALYSIS	32
	Shaker Table Experiment Without Damping	32
	Shaker Table Experiment With Damping	34
	Impulse Testing Experiment	34
	Finite Element Analysis – Unconstrained Condition	34
	Sting – Only Configuration	34
	Tetrahedron Meshes	34
	Quadrilateral Meshes	37
	Sting + Nut Configuration	37
	Sting + Nut + Balance and Calibration Device Configuration	39
	Finite Element Analysis – Constrained Condition	39

Sting-Only Configuration.....	39
Sting + Nut Configuration.....	42
Sting + Nut + Balance and Calibration Device Configuration.....	44
Comparison of Mode Shapes from Constrained and Unconstrained Condition.....	44
V. CONCLUSIONS AND RECOMMENDATIONS	49
BIBLIOGRAPHY	50
APPENDICES	53
VITA.....	66

LIST OF TABLES

Table 1: Configuration for Shaker Table Experiment with Damping	18
Table 2: Comparison of Mode Extraction Methods in ANSYS [7]	22
Table 3: Results Summary for Impulse Testing Experiment.....	37
Table 4: Results Summary for Tetrahedron Meshes	37
Table 5: Results Summary for Quadrilateral Meshes.....	38
Table 6: Results from the Sting + Nut Configuration.....	38
Table 7: Results from the Sting + Nut + Balance and Calibration Device Configuration	39
Table 8: Results Summary for Sting Only Meshes – Constrained Condition	41
Table 9: Results Summary for Sting + Nut Mesh – Constrained Condition	43
Table 10: Results Summary for Sting + Nut + Balance and Calibration Device Mesh – Constrained Condition	45
Table 11: Results comparison for Sting + Nut + Balance and Calibration Device Configuration	46
Table E-1: Results Comparison For Sting Only Configuration – Tetrahedron Mesh	63
Table E-2: Results Comparison For Sting Only Configuration – Quadrilateral Mesh....	64
Table E-3: Results Comparison for Sting + Nut Configuration	65

LIST OF FIGURES

Figure 1: Generic Model Support System [1].....	2
Figure 2: Spring and Mass System [1].....	3
Figure 3: Vibration Attenuation at the Model Eigenfrequencies [1]	4
Figure 4: Model Support System [2]	5
Figure 5: Cross Section of Movable Arc Sector [2]	5
Figure 6: Vertical Stiffening Rods-In and Rods-Out Configurations [3]	6
Figure 7: Model with Vertical Stiffening Rods Installed [3].....	7
Figure 8: 1 st 3 Modes of a Cantilevered Beam Vibrating in the Transverse Direction [6]	8
Figure 9: Autocad Drawing of the Sting.....	10
Figure 10: Autocad Drawing of the Balance	11
Figure 11: Autocad Drawing of the Calibration Device (or model).....	11
Figure 12: Balance and Calibration Device	12
Figure 13: Autocad Drawing of the Nut	12
Figure 14: Complete Model	12
Figure 15: End View Drawing of Sleeve.....	13
Figure 16: Drawing of Sleeve – Section View AA	13
Figure 17: Drawing of Sleeve – Section View BB.....	13
Figure 18: Assembly Diagram of Equipment Used in Shaker Table Experiment.....	14
Figure 19: Model Clamped on Shaker Table.....	15
Figure 20: Shaker Table Clamp	15
Figure 21: Sleeve	16
Figure 22: V-Block	17
Figure 23: Model Clamped on Shaker Table.....	18
Figure 24: Accelerometer Locations Along Model	18
Figure 25: Vibration Analysis Hardware	20
Figure 26: Assembly Diagram of Components in Impulse Testing Experiment.....	20
Figure 27: Solid 45 Element [7]	22
Figure 28: Tet Mesh 1	24
Figure 29: Tet Mesh 2.....	24
Figure 30: Tet Mesh 3.....	24
Figure 31: Tet Mesh 4.....	25
Figure 32: Quad Mesh 1	26
Figure 33: Quad Mesh 2	26
Figure 34: Quad Mesh 3	26
Figure 35: Sting + Nut Configuration – Finite Element Model.....	28
Figure 36: Sting + Nut + Balance and Calibration Device Configuration – Finite Element Model	28
Figure 37: Sting Only Tetrahedron Mesh for Constrained Condition – View 1	29
Figure 38: Sting Only Tetrahedron Mesh for Constrained Condition – View 2	29
Figure 39: Sting Only Quadrilateral Mesh for Constrained Condition – View 1	30
Figure 40: Sting Only Quadrilateral Mesh for Constrained Condition – View 2.....	30
Figure 41: Sting + Nut Mesh for Constrained Condition	31

Figure 42: Sting + Nut + Balance and Calibration Device Mesh for Constrained Condition – Constrained End Only.....	31
Figure 43: Frequency Plot of Sting Only Configuration	32
Figure 44: Frequency Plot of the Sting + Nut Configuration	33
Figure 45: Frequency Plot of Sting + Nut + Balance Configuration	33
Figure 46: Results from Sting Accelerometer for Low Frequency Range	35
Figure 47: Results from Balance Accelerometer for Low Frequency Range	35
Figure 48: Frequency Plot for Sting Only Configuration – Trial 1	36
Figure 49: Frequency Plot for Sting + Nut Configuration – Trial 1	36
Figure 50: Frequency Plot for Sting + Nut + Balance Configuration – Trial 1	36
Figure 51: Sting Only Tetrahedron Mesh for Constrained Condition – Plot of 1 st Mode Shape (distorted)	40
Figure 52: Sting Only Tetrahedron Mesh for Constrained Condition – Plot of 2 nd Mode Shape (distorted)	40
Figure 53: Sting Only Tetrahedron Mesh for Constrained Condition – Plot of 3 rd Mode Shape (distorted)	40
Figure 54: Sting Only Quadrilateral Mesh for Constrained Condition – Plot of 1 st Mode Shape (distorted)	41
Figure 55: Sting Only Quadrilateral Mesh for Constrained Condition – Plot of 2 nd Mode Shape (distorted)	41
Figure 56: Sting Only Quadrilateral Mesh for Constrained Condition – Plot of 3 rd Mode Shape (distorted)	41
Figure 57: Sting + Nut Mesh for Constrained Condition – Plot of 1 st Mode Shape (distorted).....	42
Figure 58: Sting + Nut Mesh for Constrained Condition – Plot of 2 nd Mode Shape (distorted).....	42
Figure 59: Sting + Nut Mesh for Constrained Condition – Plot of 3 rd Mode Shape (distorted).....	43
Figure 60: Sting + Nut + Balance and Calibration Device Mesh for Constrained Condition Plot of 1 st Mode Shape (distorted)	45
Figure 61: Sting + Nut + Balance and Calibration Device Mesh for Constrained Condition Plot of 2 nd Mode Shape (distorted)	45
Figure 62: Sting + Nut + Balance and Calibration Device Mesh for Constrained Condition Plot of 3 rd Mode Shape (distorted).....	45
Figure 63: 1 st Mode Shape for Constrained Condition (distorted)	46
Figure 64: 2 nd Mode Shape for Constrained Condition (distorted)	46
Figure 65: 1st Mode Shape for Unconstrained Condition (distorted)	47
Figure 66: 3 rd Mode Shape for Constrained Condition (distorted).....	47
Figure 67: 2 nd Mode Shape for Unconstrained Condition (distorted)	47
Figure 68: 4 th Mode Shape for Constrained Condition (distorted).....	47
Figure 69: 3 rd Mode Shape for Unconstrained Condition (distorted).....	47
Figure 70: 5 th Mode Shape for Constrained Condition (distorted).....	48
Figure 71: 4 th Mode Shape for Unconstrained Condition (distorted).....	48
Figure A-1: System for Measuring Deflection with Laser Light Source	54
Figure B-1: Option 1 for Producing Deflection in a Beam with a Cell Phone Motor	55

Figure B-2: Option 2 for Producing Deflection in a Beam with a Cell Phone Motor	55
Figure C-1: Calculations for Beam Size	56
Figure D-1: Autocad Drawing of Sting	60
Figure D-2: Autocad Drawing of Balance	61
Figure D-3: Assembly Drawing of Model Components.....	62

LIST OF ABBREVIATIONS

Degrees of freedom.....	DOF
Hertz.....	Hz
Inch.....	in
Ounce.....	oz
Pound.....	lb
Pounds per square inch.....	psi
Radians per second.....	Rad/sec
Revolutions per minute.....	Rpm
Second.....	sec

CHAPTER 1

INTRODUCTION

A number of wind tunnel test facilities are experiencing undesirable vibrations of the model support system. A generic model support system is shown in Figure 1. These vibrations lead to a number of problems. For example, when the model vibrates, the test conditions are no longer realistic. The dynamics of the model and sting cause the flow to become unsteady. The data collected from unsteady flow differs from that collected when the flow is steady state. Another major concern is that the vibrations could cause the model to come apart and damage components inside the wind tunnel, such as compressors or blades, which could be costly to repair. Therefore, limitations are placed on the conditions at which the tunnel can be operated.

This situation is not unprecedented. Similar problems have been experienced in the European Transonic Wind Tunnel in Germany and the National Transonic Facility at the NASA Langley Research Center. These facilities arrived at different solutions to the problem, which will be discussed in greater detail in the next section of this paper.

Wind tunnel vibration problems are not unlike vibration problems associated with any mechanical system or noise in an electronic circuit. Therefore, principles such high pass and low pass filtering and both active and passive damping could be applied to the wind tunnel vibration problem. Examples of passive damping include using a material with different damping properties or changing the mass of the system (if this is an option). An example of active damping would be using an interface with piezoceramics to control the vibration.

In order to reduce the vibrations in the wind tunnel, the vibration must first be measured, which will be the primary topic of this paper. The purpose of this thesis was to design a generic model support system that closely represents a typical wind tunnel model support system (sting, balance, and a generic model), measure the vibration in the model support system, perform modal analysis, and compare the results with finite element modeling. Passive damping techniques were also explored experimentally.

Several experimental methods were considered as options to measure deflection of a vibrating beam. This study utilizes a cylindrical beam as a simplification of the sting problem. Two experiments were conducted, and the finite element solutions obtained were consistent with the results from the experiments.

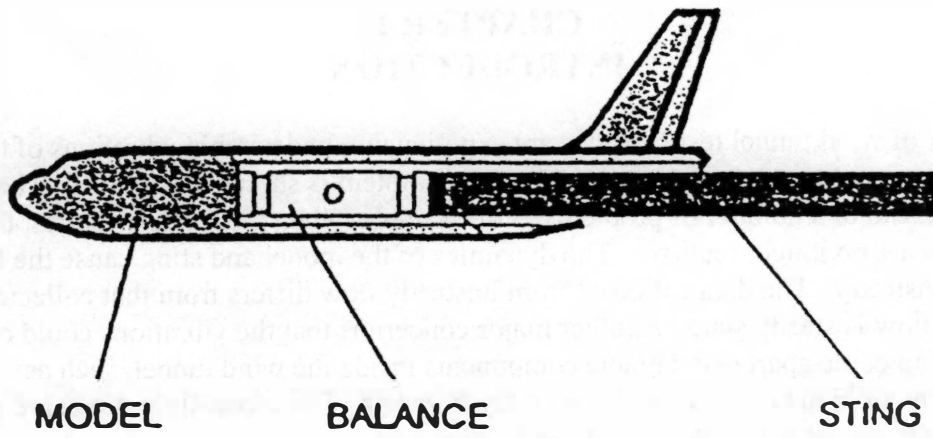


Figure 1: Generic Model Support System [1]

CHAPTER 2 LITERATURE REVIEW AND BACKGROUND

Literature Review

As noted earlier, a number of solutions to wind tunnel vibration problems have been proposed and developed. Among the solutions are techniques that include using piezoceramic elements to attenuate vibration [1], using a different bearing surface material with a lower coefficient of friction [2], using bump stops to limit the vibration [2], and using vertical stiffening rods [3]. Piezoelectric devices have also been used in several other vibration applications, such as vibration suppression of shells and plates [4] and buffet loads alleviation [5]. The above-mentioned solutions will be discussed in the following five case studies.

Case Study 1

An anti-vibration system (AVS) was developed for the European Transonic Windtunnel to counteract vibration at the eigenfrequencies of the model/balance assembly [1]. In many cases, vibration results from the model support system, but this was not the case at the European Transonic Windtunnel. Measurements showed that the system causing vibration could be described as a spring and mass system that consisted of the balance and model arrangement, as shown in Figure 2. The vibration particularly affected their ability to measure the angle of attack of the model [1].

In order to attenuate the vibrations experienced at the ETW, an active vibration suppression system was installed between the sting and balance. The AVS consisted of an active interface with piezoceramic elements, power amplifiers, and a digital control system. Vibration was suppressed by elongating piezoceramic elements. Validation tests concluded that vibration attenuation was only successful in the regions of the model eigenfrequencies, as shown in Figure 3 [1].

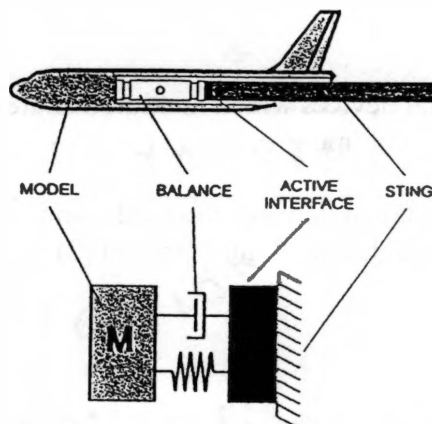


Figure 2: Spring and Mass System [1]

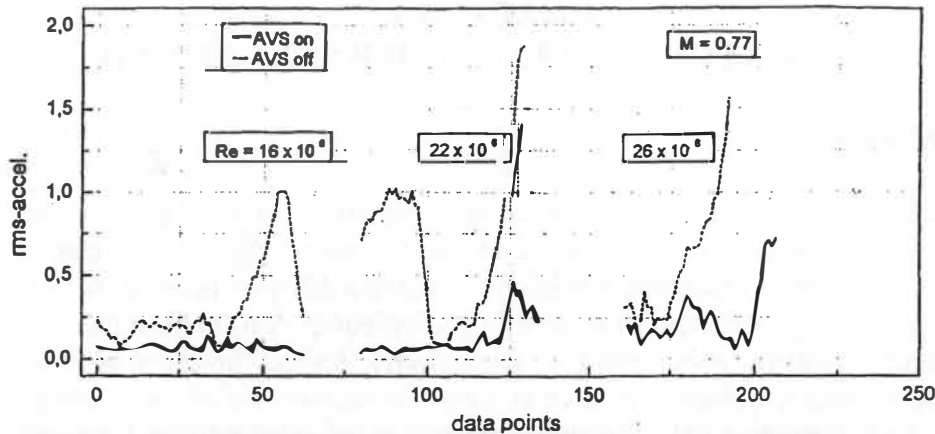


Figure 3: Vibration Attenuation at the Model Eigenfrequencies [1]

Case Study 2

A study was conducted in the National Transonic Facility at the NASA Langley Research Center to explore the dynamic interaction between the model support structure and the model. The model support structure can be seen in Figure 4. Prior to this test, a new bearing surface material was installed on the bearings of the arc sector, which allows for pitch movement, in an effort to reduce the yaw vibration. This new material had a lower coefficient of friction and allowed the bearings to fit snugly against the arc sector; therefore, the arc sector was able to move more smoothly. The arc sector is shown in Figure 5. Tests showed that this new material attenuated yaw vibration on several models. However, during future tests, the yaw vibration was still present. This was unexpected, since the new bearing surface material had proved to reduce the yaw vibrations. Results indicated that extreme yaw vibrations were occurring as a result of the yaw mode natural frequency of the model coinciding with that of the model support structure and that the yaw vibration was linked to the vibration of the model support system. These yaw vibrations were causing problems such as [2]:

- Costly model loss
- Damage to the facility
- Reduced data quality
- Bias errors in the inertial devices which measured angle of attack
- Inefficient wind tunnel run time

Therefore, bump stops were installed between the model and the sting in the yaw plane. Bump stops serve to limit the amplitude of the vibration [2].

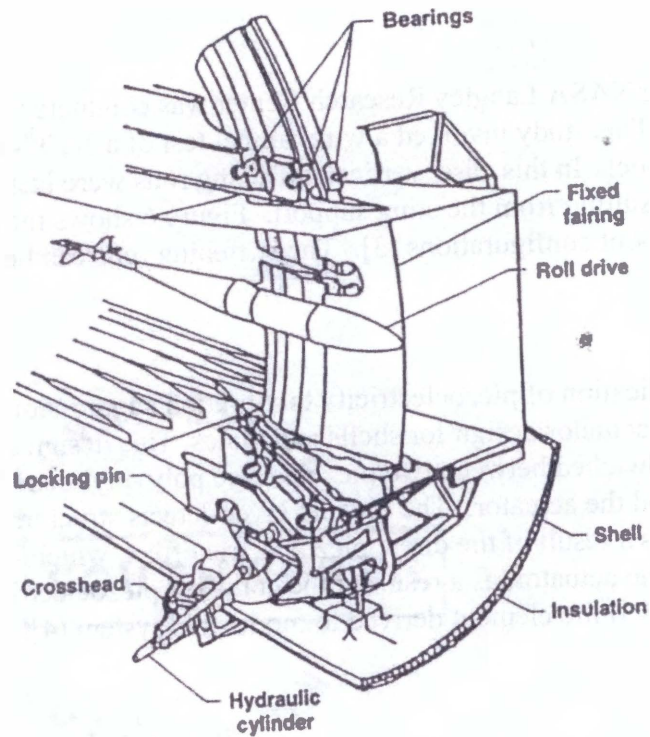


Figure 4: Model Support System [2]

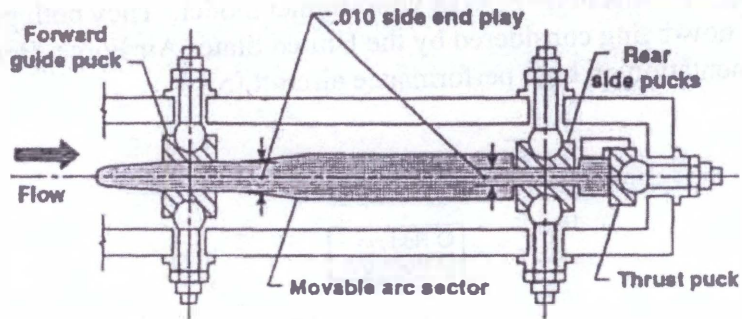


Figure 5: Cross Section of Movable Arc Sector [2]

Case Study 3

Another study at the NASA Langley Research Center was conducted in the Transonic Dynamics Tunnel. This study involved a wind tunnel test of a 1/10th-scale Atlas-Centaur 1 launch vehicle model. In this case, vertical stiffening rods were installed in the sting to reduce vibrations resulting from the sting support. Figure 6 shows the difference between the rods-in and rods-out configurations [3]. The stiffening rods can be seen in Figure 7.

Case Study 4

A more general application of piezoelectricity to vibration suppression involves a piezoelectric sensor/actuator design for shells and plates. This design consisted of a plexiglass plate sandwiched between two piezoelectric polyvinylidene fluoride layers, the distributed sensor and the actuator. The sensing layer detects structural vibration and produces a charge, as a result of the direct piezoelectric effect, which is then converted into a deflection of the actuator, as a result of the converse piezoelectric effect. This study describes a new finite element derived to model this system [4].

Case Study 5

Buffet loads alleviation is another application of piezoelectricity. Two new piezoelectric actuators were developed and tested in the Transonic Dynamics Tunnel. One of the actuators was the Macro-Fiber Composite actuator developed at the NASA Langley Research Center, and the other was the Active Fiber Composite actuator developed at the Continuum Control Corporation. These actuators contained interdigitated electrodes and were embedded into the fins of an F/A-18 wind-tunnel model. They both performed well in the test and are now being considered by the United States Air Force, Boeing, and NASA for implementation on high performance aircraft [5].

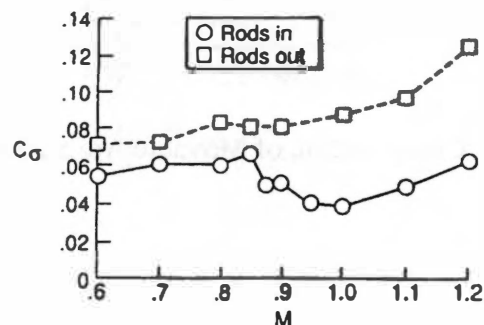


Figure 6: Vertical Stiffening Rods-In and Rods-Out Configurations [3]

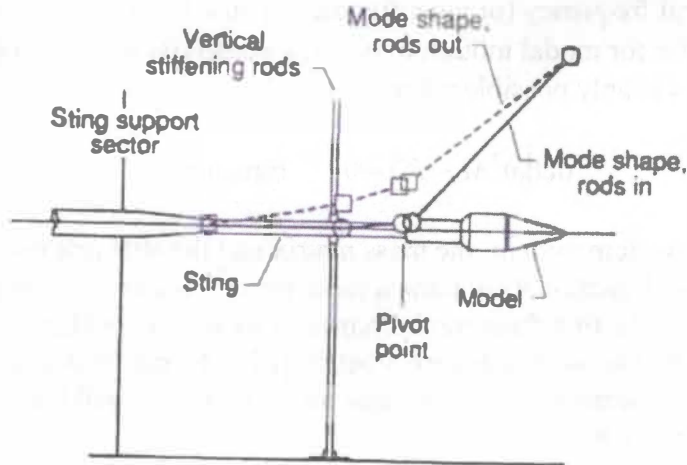


Figure 7: Model with Vertical Stiffening Rods Installed [3]

Background

What is modal analysis?

Modal analysis is a type of analysis used to determine the natural frequencies and mode shapes of structural and mechanical systems. It is useful in vibration analysis, diagnosis, and design. For example, malfunction or failure of a system may be due to excitation of one of its natural frequencies. Therefore, using modal analysis, a system can be designed such that it will not be subject to vibrations (or significantly reduce vibrations) in the ranges where its natural frequencies occur, thereby avoiding potential malfunction. It can also be used to locate severe vibration in a system [6].

Modal Analysis Theory

The differential equation for a linear, lumped-mass, undamped system is described by the following equation: [6]

$$M\ddot{y} + Ky = f(t) \quad \text{Equation 1}$$

where y is the displacement vector, f is the force vector, M is the mass matrix, and K is the stiffness matrix. Since displacement vectors have harmonic motions at specific frequencies, they can be expressed by the following equation: [6]

$$y = \psi \cos \omega t = \psi e^{j\omega t} \quad \text{Equation 2}$$

Modal analysis requires the solution to the eigenvalue problem in Equation 3 [6], which results from the combination of Equations 1 and 2.

$$[\omega^2 M - K]\Psi = 0 \quad \text{Equation 3}$$

where ω is the natural frequency (or eigenfrequency) and Ψ is the mode shape (or eigenvector). In order for modal motion to occur, a nontrivial solution for Ψ must exist (i.e. $\Psi \neq 0$) [6]. This is only possible when

$$\det[\omega^2 M - K] = 0 \quad \text{Equation 4}$$

For an n-degree of freedom system, the mass matrix and the stiffness matrix are both square matrices; thus, Equation 4 contains n roots for ω^2 . For each natural frequency, ω_i , a mode shape exists. The first three mode shapes of a cantilevered beam vibrating in the transverse direction can be seen in Figure 8 below [6]. The model discussed in this paper could be modeled as a beam with a point mass on the end, so it will have mode shapes similar to those in Figure 8.

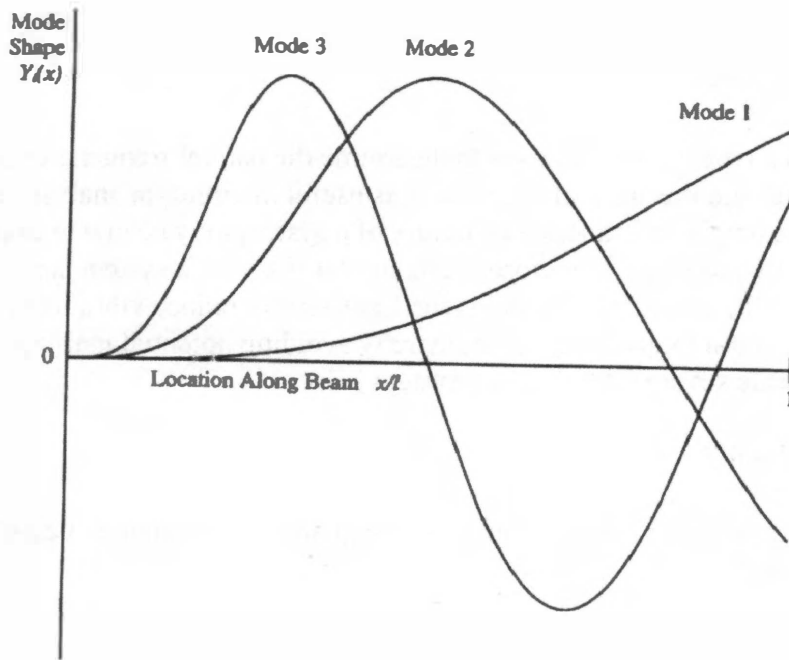


Figure 8: 1st 3 Modes of a Cantilevered Beam Vibrating in the Transverse Direction [6]

CHAPTER 3 EXPERIMENTAL APPROACH

Dynamic deflection (or vibration) can be measured in a variety of ways. Options considered in this experiment are listed below.

- Strain Gage
- Accelerometer
- Optics (video or lasers)

Strain gages and accelerometers are commonly used to measure dynamic deflection. They are inexpensive, easily obtained, and can be attached with adhesive. In addition, if they are calibrated correctly, they are very accurate. Optics, which is less conventional, was another option considered because it offers an advantage over the strain gage and accelerometer. Unlike a strain gage or accelerometer, neither a video camera nor a laser would have to come in contact with the model; therefore, the model would not be altered in any way. Another advantage is that the deflection could simply be measured with a caliper. For measurement with a laser light source, the configuration shown in Figure A-1 in Appendix A and the discussion that follows was considered. However, because of the convenience and availability of accelerometers, they were chosen as the instrument to measure vibration in the following experiments.

Several possibilities existed as potential mechanisms to drive the vibration. These included a small cell phone motor and the shaker table in the University of Tennessee Space Institute laboratory. Three configurations were considered for use with the cell phone motor. Two of these configurations can be seen in Figures B-1 and B-2 in Appendix B. The third configuration would be to simply mount the motor inside of a hollow beam, so that the vibration of the motor would vibrate the beam.

Because the sting is cylindrical in shape, a cylindrical beam was chosen as the shape of the model. Both solid and hollow cylindrical beams as well as beams made of different materials were considered. In order to use the cell phone motor, a very small and lightweight beam would have to be used because of the size of the motor. Given that the motor had a frequency of 10,000 rpm, calculations were made to determine an appropriate beam size for a solid steel beam, hollow steel beam, and a hollow copper beam to be used in conjunction with the motor. These calculations can be found in Figure C-1 in Appendix C. (Red indicates the best of the acceptable solutions. Green indicates unacceptable solutions because the frequency is greater than 10,000 rpm.) On the other hand, the shaker table could handle most any size beam; it has a useful frequency range of 5 Hz - 3000 Hz (approximately 31 rad/sec to 18,850 rad/sec). Also, using the motor would require a custom fabricated beam, and a commercially available beam would be sufficient for use with the shaker table. Therefore, the shaker table was chosen as the instrument to drive the vibration. A hollow configuration was chosen for the shape of the model, because a sting found inside of a wind tunnel houses the electrical wires from the balance.

Model Design

The components of the generic model for the two experiments discussed later include: a sting, a balance, and a “model”. The sting is a 54-inch long hollow cylinder made of carbon steel, with inner and outer diameters of 0.375 inches and 1 inch, respectively. The weight of the sting is 10.4 lbs. The length of the beam (54 inches) allows for 6 inches going into the clamp for support and 48 inches for vibration. This size was chosen because it has a natural frequency of approximately 11 Hz, which is in a range where problems are commonly experienced in wind tunnels. The balance is also made of carbon steel. For the purposes of these experiments, a simplified version of an actual balance was used, which includes no instrumentation. The “model” is actually a calibration device, which can support weights in different locations. The calibration device represents a wind tunnel model, such as an airfoil or any part of an airplane. By adding weights in different locations, the distribution of mass can be adjusted. The balance is actually located inside of the calibration device, similar to a typical configuration. The weight of the balance and calibration device is 2.7 lbs. The sting is connected to the balance by a nut (11.8 oz), and pins connect the balance and calibration device. In addition to the model components described above, an aluminum sleeve was designed as a means of passive damping. The weight of the sleeve is 1.8 lbs. This sleeve clamps onto the sting to change the frequency response of the system. Drawings and images of the model components can be seen in Figures 9 – 17 below. A larger image of Figures 9 and 10 as well as an assembly drawing of the model components can be found in Figures D-1, D-2, and D-3 in Appendix D.

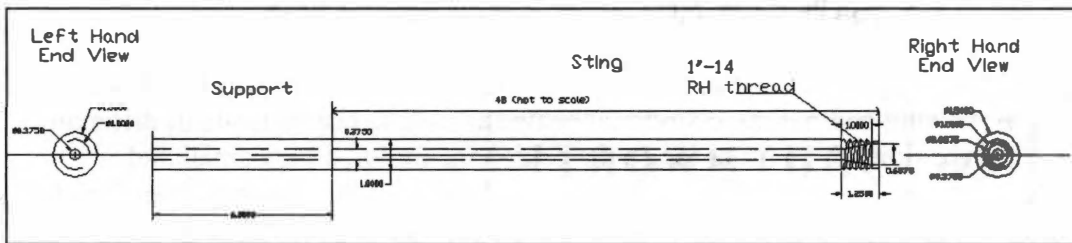


Figure 9: Autocad Drawing of the Sting

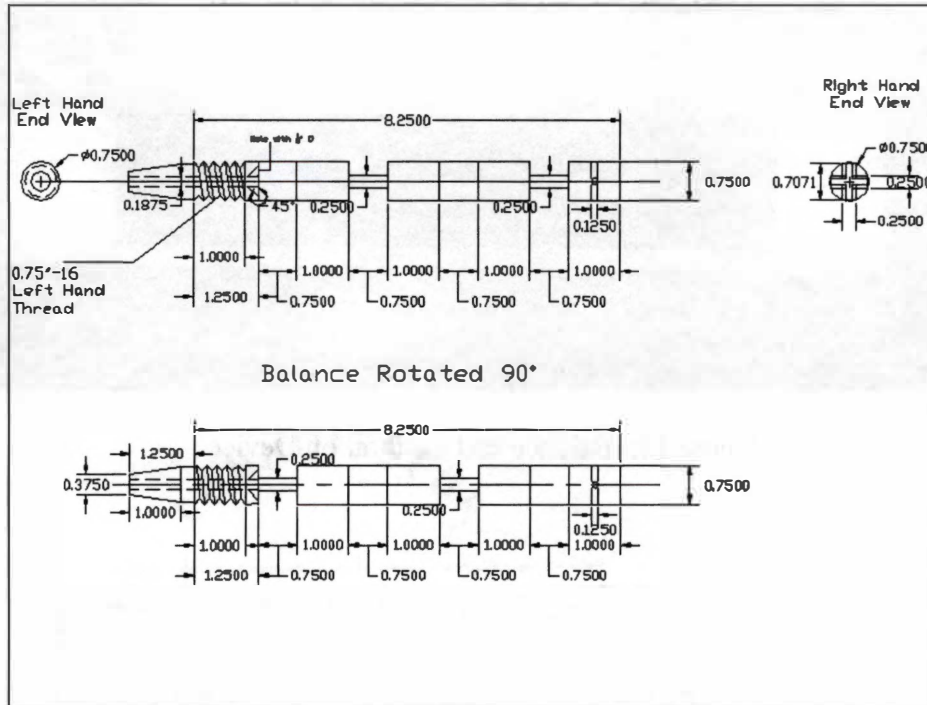


Figure 10: Autocad Drawing of the Balance

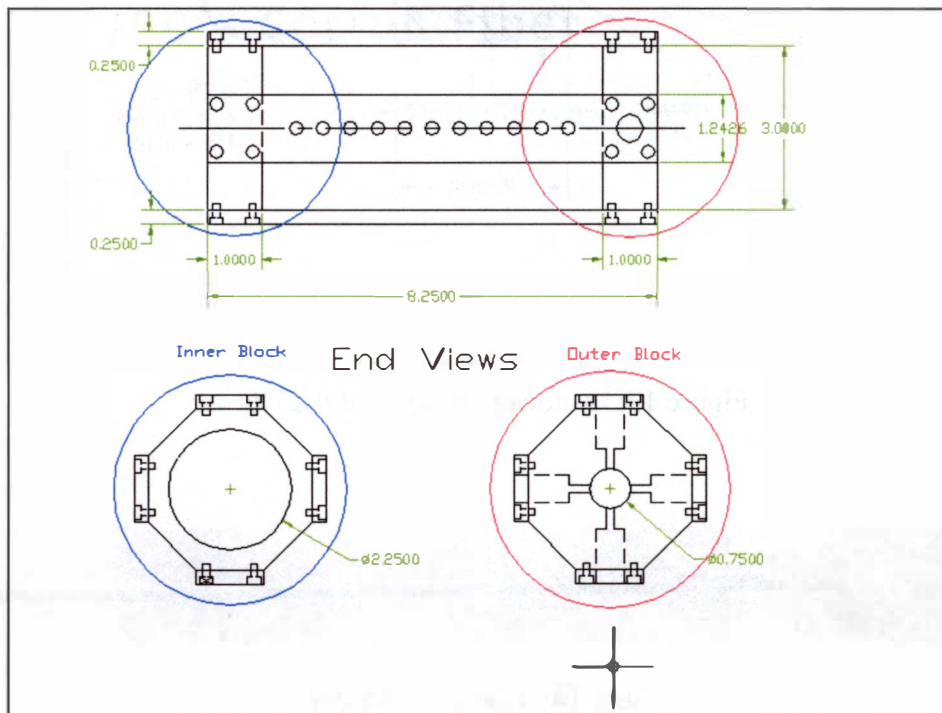


Figure 11: Autocad Drawing of the Calibration Device (or model)

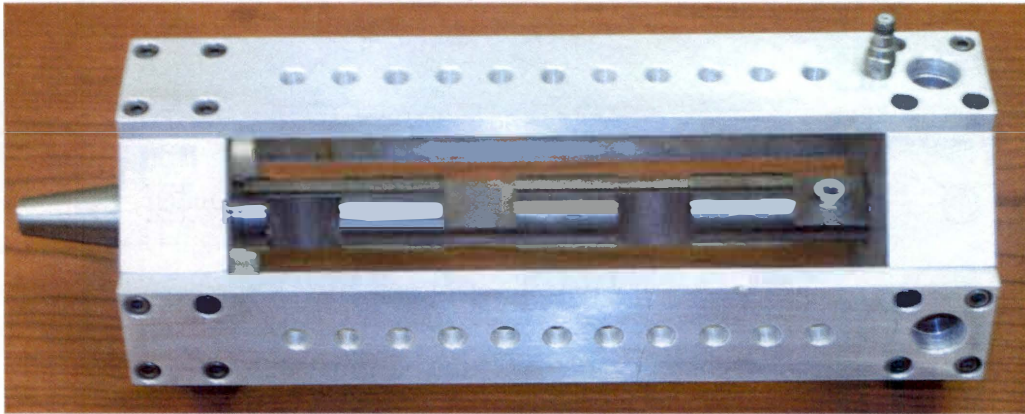


Figure 12: Balance and Calibration Device

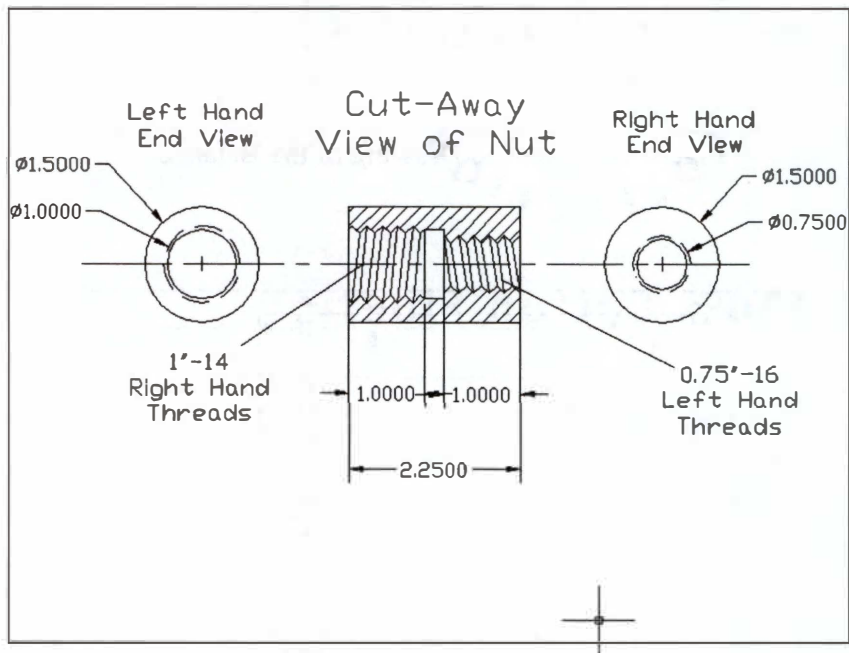


Figure 13: Autocad Drawing of the Nut



Figure 14: Complete Model

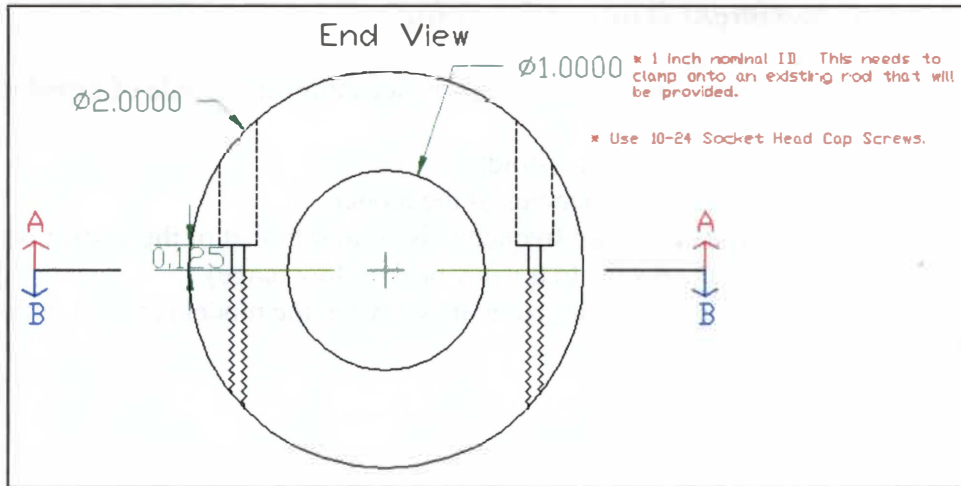


Figure 15: End View Drawing of Sleeve

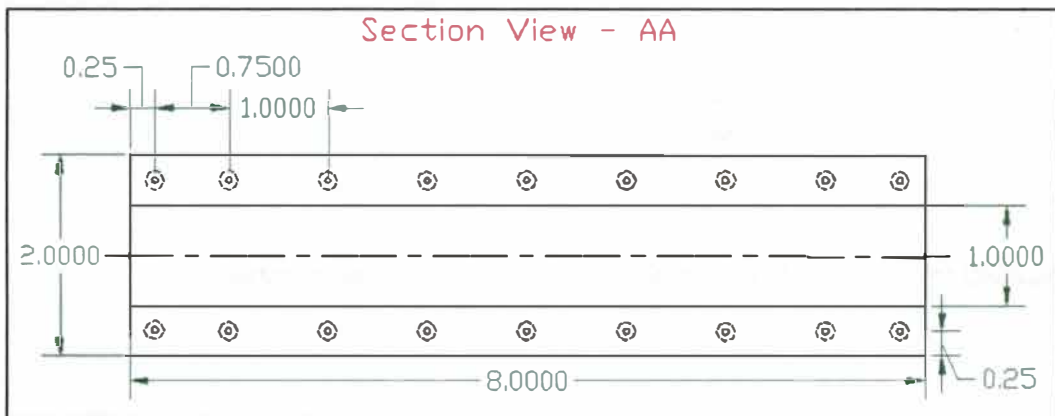


Figure 16: Drawing of Sleeve – Section View AA

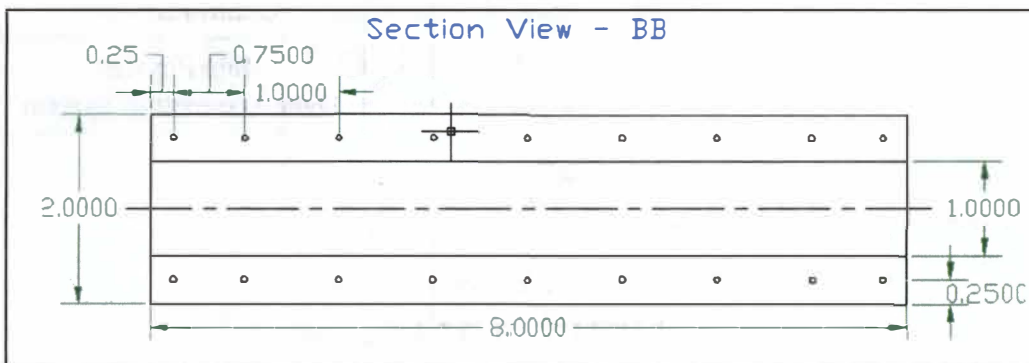


Figure 17: Drawing of Sleeve – Section View BB

Shaker Table Experiment Without Damping

The model in this experiment was constrained using a cantilevered mode of installation.

The purpose of this experiment was three-fold:

1. To determine the natural frequencies of the model.
2. To ensure the first fundamental frequency is similar to that of the system being modeled (generic system with frequency peak in low range).
3. To establish a baseline for future comparison when the model is tested with damping material.

Equipment List and Setup

Equipment List

- Ling Shaker table (Model B335)
- 4 PCB accelerometers (Model 353B18)
- The model (sting, nut, balance, and calibration device)
- Ling Power Amp
- Signal Conditioner
- Data Physics Control System
- Data Physics Data Acquisition System

Setup

The diagram in Figure 18 below explains how the equipment operated.

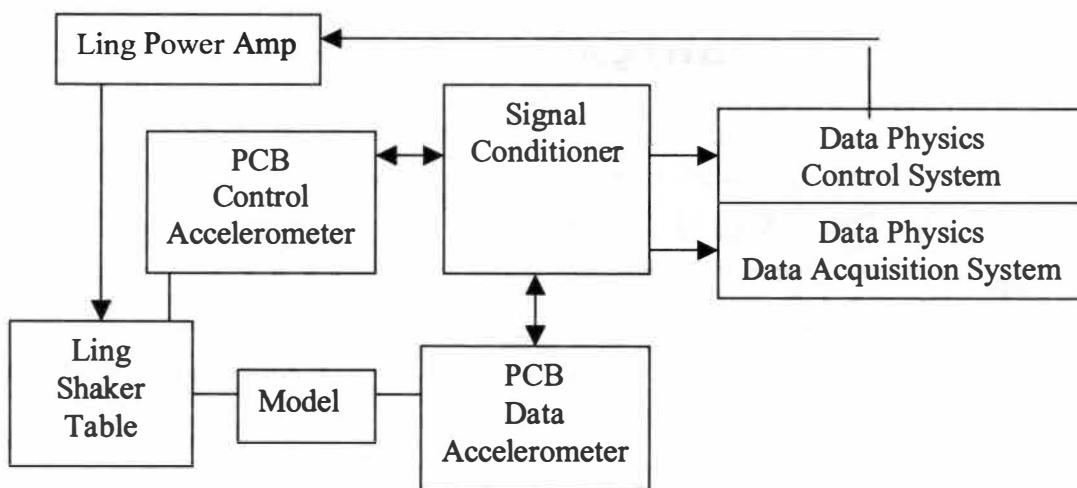


Figure 18: Assembly Diagram of Equipment Used in Shaker Table Experiment.

Procedure

The model was placed into a clamp connected to the shaker table, where 2.67 in of the sting went into the clamp. The shaker table was set to sweep a frequency range of 7 Hz to 100 Hz. Because the shaker table data acquisition system contains three channels, three accelerometers were placed along the beam. They were located in the center of the sting, on the end of the sting next to the nut, and on the calibration device above the end of the balance. A fourth accelerometer was attached to the shaker table for control. The accelerometer locations correspond to the points of maximum deflection for the first three modes of vibration. Data was collected on three different configurations – the sting only, the sting plus the nut, and the sting plus the nut plus the balance and calibration device. This was to investigate the source of the critical part of the frequency. For example, the frequencies of the sting only configuration and the sting plus nut configuration were expected to be similar; therefore, the nut would not be a critical component of the system. Each trial was videotaped to capture the frequency mode shapes. Figures 19 and 20 below illustrate the model setup.

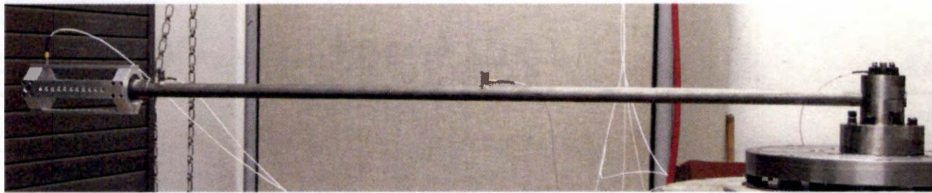


Figure 19: Model Clamped on Shaker Table

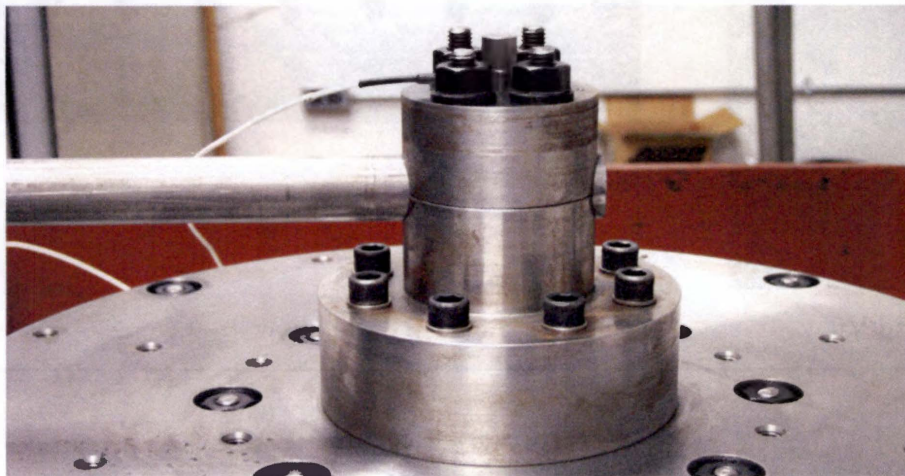


Figure 20: Shaker Table Clamp

Shaker Table Experiment With Damping

The model in this experiment was constrained using a cantilevered mode of installation.

The purpose of this experiment was two-fold:

1. To determine the natural frequencies of the model with passive damping included.
2. To compare the results with those of the same experiment with no damping.

Equipment List and Setup

The equipment list and setup for this experiment were the same as in the Shaker Table Experiment without damping, with the addition of the following components:

- An 8-inch circular aluminum sleeve
- A 6x6x2 inch steel v-block
- 2 pieces of 8 inch long rubber with 1/32 inch thickness
- A piece of a plastic zip-lock bag

The sleeve and the v-block can be seen in Figures 21 and 22 below.

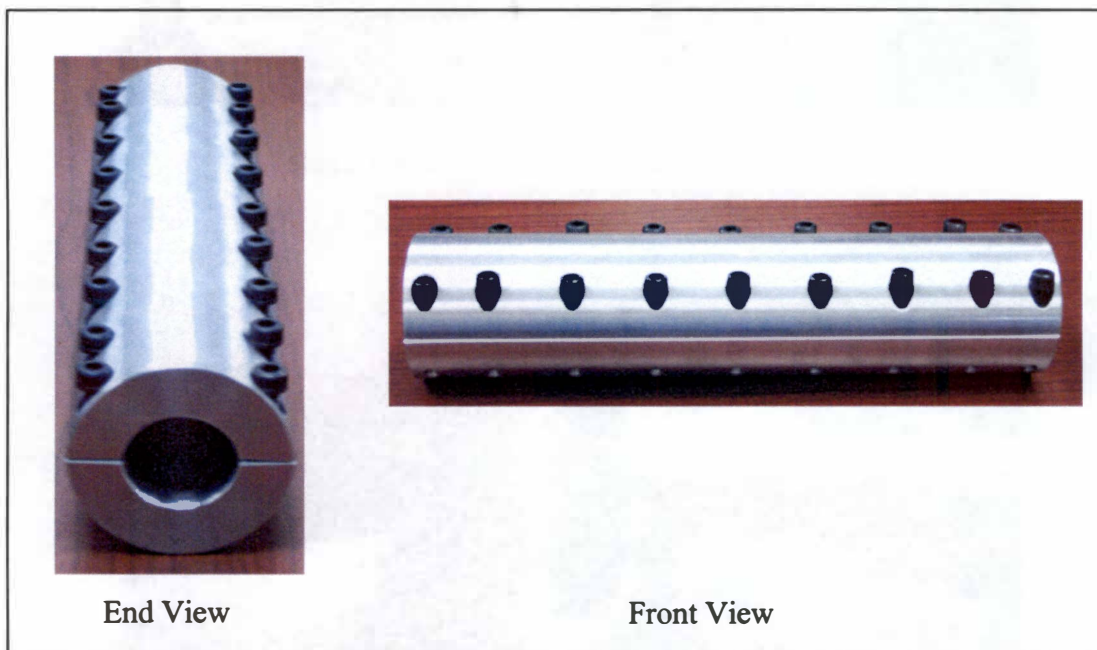


Figure 21: Sleeve

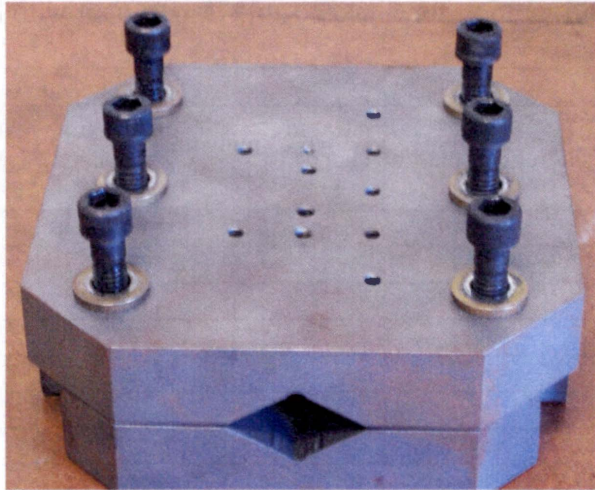


Figure 22: V-Block

Procedure

The model was placed into a clamp connected to the shaker table, where 2.7 inches of the sting went into the clamp as before. The shaker table was set to sweep a frequency range of 5 Hz to 100 Hz. Two accelerometers were placed along the model, one at the end of the sting next to the nut and the other on the end of the balance. A third accelerometer was attached to the shaker table for control as before.

Data was collected on eleven different configurations, with the difference between the configurations being the sleeve or v-block location and the addition of rubber or plastic between the sleeve and the sting. No damping material was tested with the v-block. The eleven configurations are shown in Table 1. This was to investigate at what location damping would be most effective and whether or not material such as plastic or rubber would affect the results. Based on previous research, it was expected that the sleeve and v-block would greatly affect the frequency response. This was important in order to shift the first frequency peak out of the low frequency range that is a problem. Figures 23 and 24 below illustrate the experiment setup.

Impulse Testing Experiment

The purpose of this experiment was two-fold:

1. To determine the natural frequencies of the model.
2. To establish a baseline for future comparison when the model is tested with passive damping.

Unlike in the shaker table experiment, the model in this experiment was unconstrained.

Table 1: Configuration for Shaker Table Experiment with Damping

Configuration	sleeve	v-block	rubber	plastic	Location				
					next to clamped end	midpoint of sting	25% from clamped end	1/3 the length of the sting	next to accelerometer on end of sting
1									
2	x				x				
3	x					x			
4	x						x		
5	x							x	
6	x								x
7	x			x				x	
8		x				x			
9		x					x		
10	x		x			x			
11	x		x				x		

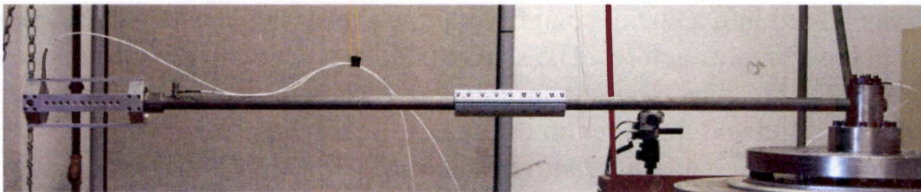


Figure 23: Model Clamped on Shaker Table

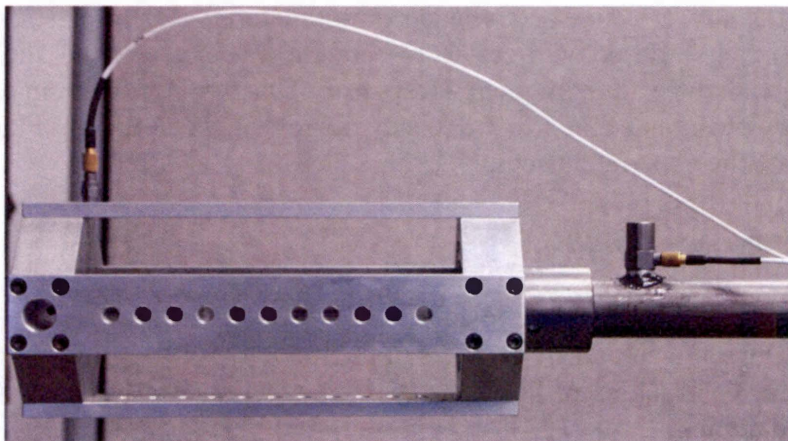


Figure 24: Accelerometer Locations Along Model

Equipment List and Setup

Equipment List

- Model (sting, nut, balance, and calibration device)
- Hammer
- PCB Accelerometer (Model 353B17)
- DSPT Siglab software (version 3.2.4)
- Computer with Matlab installed
- Siglab Hardware Measurement Module (Siglab HMM)
- PCB Power Supply for Accelerometer (PCB PS-Accel)
- Power Supply for Hammer Accelerometer (PS-Hammer Accel)

Figure 25 shows the vibration analysis hardware.

DSPT Siglab is a vibration analysis software package that communicates with Matlab to produce plots in the frequency domain or time domain.

Setup

The diagram in Figure 26 shows how the components in the Impulse Testing Experiment work together.

Procedure

The model was suspended from the ceiling with fishing line; two loops of fishing line were hung from the ceiling, and the ends of the model were placed in the loops, such that the model hung parallel to the floor. The model had an accelerometer attached to it, and it received an impact from the hammer. Upon impact, a data reading was taken. For each trial, three data readings were taken, and they were averaged.

As in the shaker table experiment, three configurations were tested - the sting only, the sting plus the nut, and the sting plus the nut plus the balance and calibration device. Five trials were conducted for each configuration. For all three configurations, the accelerometer was placed in the center of the sting, and the model was struck on the end of the sting near where the nut attaches.

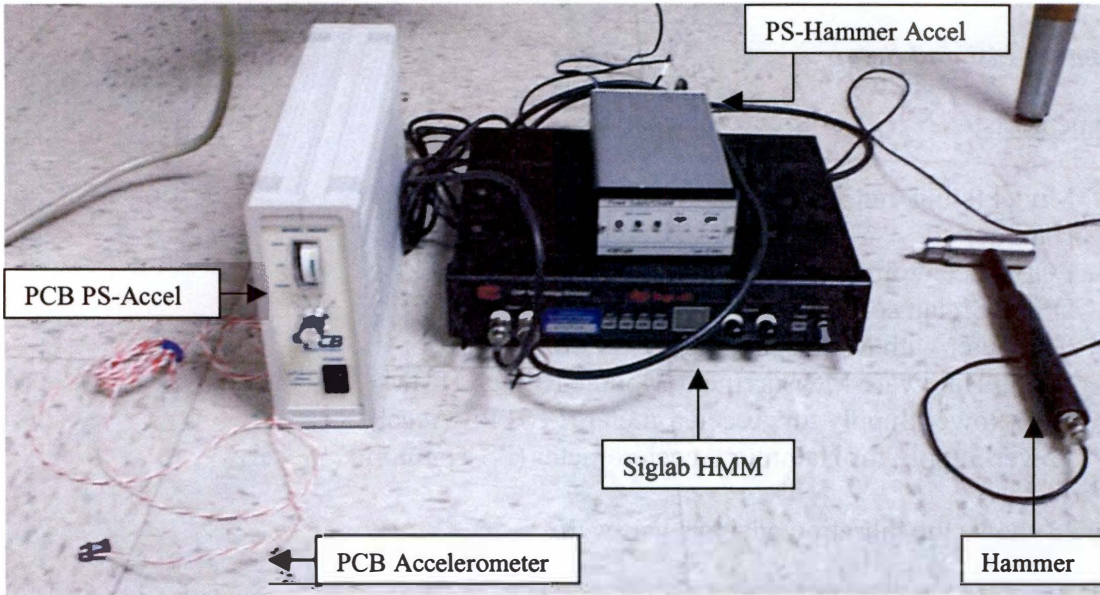


Figure 25: Vibration Analysis Hardware

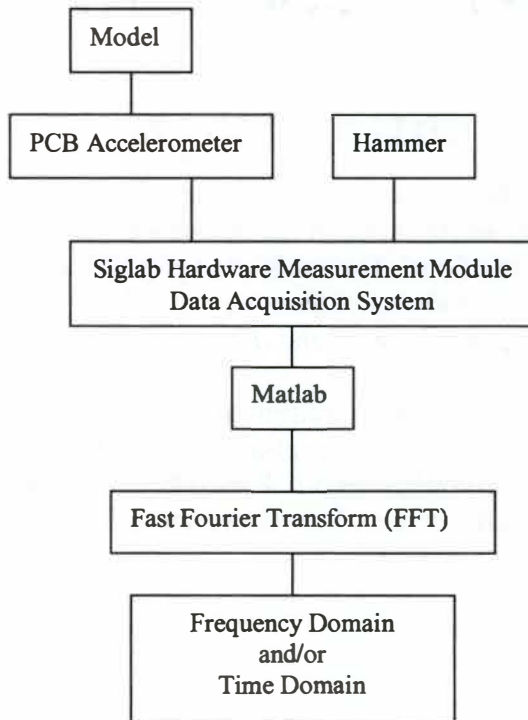


Figure 26: Assembly Diagram of Components in Impulse Testing Experiment

Finite Element Analysis

The purpose of finite element analysis is to verify the results obtained from the two experiments described above. The finite element software used was ANSYS 7.0. ANSYS has the capability to obtain a modal solution by solving the eigenvalue problem (Equation 3) using any of the following numerical methods [7]

- Block Lanczos method
- Subspace method
- PowerDynamics method
- Reduced (Householder) method

Table 2 compares these methods of mode extraction and lists some of the advantages and disadvantages of each one [7]. Both the Block Lanczos and Subspace methods were used in this analysis.

Each of the three model configurations was modeled in ANSYS, in both the constrained (as in the shaker table experiment) and unconstrained (as in the impulse testing experiment) conditions. Thus, this discussion will be divided into those two categories. The following conditions apply to all of the models in both categories.

- The material properties of steel listed below were used.
 - Modulus of Elasticity = 29,000,000 psi
 - Mass Density = $0.000747 \text{ lb} \cdot \text{s}^2 / \text{in}^4$
 - Poisson's Ratio = 0.3
- The automatic meshing feature was utilized.
- The results from each solution include both a vertical and horizontal mode. If the mesh were completely symmetric, these would be exactly the same. In most cases, the meshes were not completely symmetric, so a slight variation exists between the vertical and horizontal mode. For the purposes of comparison, only one of these modes was included in this discussion, because only one mode was measured in the experiments conducted.
- The element type used was Solid 45.

The Solid 45 element has the option of a quadrilateral or tetrahedron shape. It is a 3-D structural solid element containing eight nodes, with three DOF per node. Figure 27 is an illustration of this element [7].

Table 2: Comparison of Mode Extraction Methods in ANSYS [7]

Eigsolver	Application	Memory Required	Disk Required
Block Lanczos	Default. To find many modes (about 40+) of large models. Recommended when the model consists of poorly shaped solid and shell elements. This solver performs well when the model consists of shells or a combination of shells and solids. Works faster but requires about 50% more memory than subspace.	Medium	Low
Subspace	To find few modes (up to about 40) of large models. Recommended when the model consists of well-shaped solid and shell elements. Works well if memory availability is limited.	Low	High
Power Dynamics	To find few modes (up to about 20) of large models. Recommended for fast computation of eigenvalues of over 100K DOF models. On coarse mesh models, the frequencies are approximate. Missed modes are possible when repeated frequencies are present.	High	Low
Reduced	To find all modes of small to medium models (less than 10K DOF). Can be used to find few modes (up to about 40) of large models with proper selection of master DOF, but accuracy of frequencies depends on the master DOF selected.	Low	Low

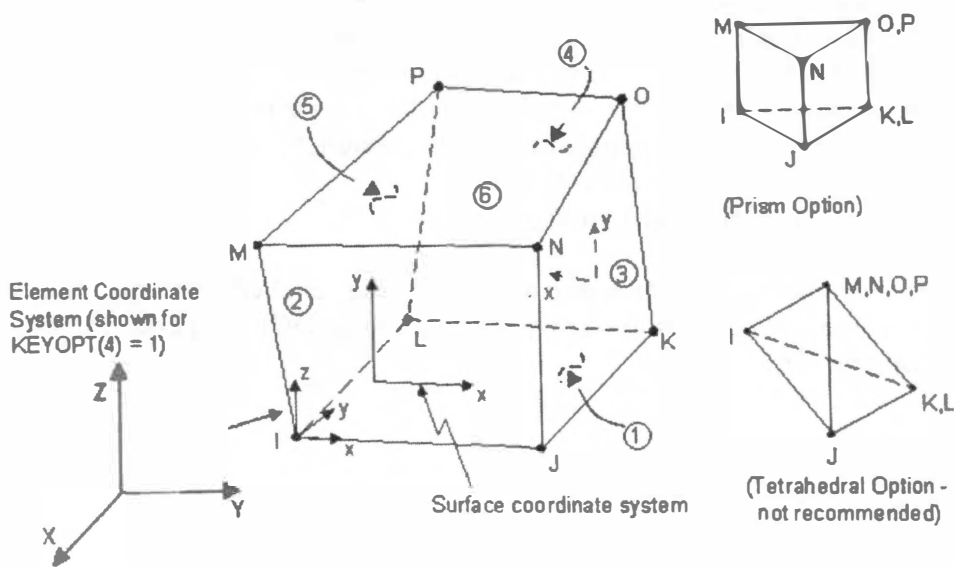


Figure 27: Solid 45 Element [7]

Unconstrained Condition

Sting Only Configuration

The sting only configuration was modeled using both quadrilateral elements and tetrahedron elements. Multiple meshes for each shape were generated, each more refined than the previous.

Some simplifications were made to the geometry in the finite element models. The physical model actually has a small taper on one end of the sting, but it was modeled as a cylinder with a uniform inner radius. This should not introduce a significant amount of error because the taper is small relative to the sting length. Also, the sting was modeled as a 48 in. beam, but it was actually 51.33 in. (a 54 in. pipe with 2.67 in. going into the clamp). Another small source of error is that the physical model is threaded on one end of the sting, but it was modeled as a smooth surface. Also, the material properties used in the finite element analysis were not exactly the same as those of carbon steel, which was the material of the model.

Tetrahedron Meshes

Tet Mesh 1

The initial tetrahedron mesh (Tet Mesh 1) consisted of 8757 elements. This mesh can be seen in Figure 28. This mesh was very course in the cross section and needed refinement. Due to the way the mesh was generated, the model did not maintain a uniform shape through the center. Also, the default settings of the automatic meshing feature in ANSYS created too many elements with poor aspect ratios.

Tet Mesh 2

Tet Mesh 1 was refined to produce Tet Mesh 2. It consisted of 30,733 elements and can be seen in Figure 29. This mesh was still rather course in the cross section, and it did not maintain a uniform shape through the center. Also, the aspect ratios were still poor. Therefore, further refinement was desired.

Tet Mesh 3

Tet Mesh 2 was refined to produce Tet Mesh 3. It consisted of 15,575 elements and can be seen in Figure 30. Aspect ratios were acceptable in this mesh. However, further refinement was needed to obtain a uniform shape through the center and increase the number of cross-sectional elements.

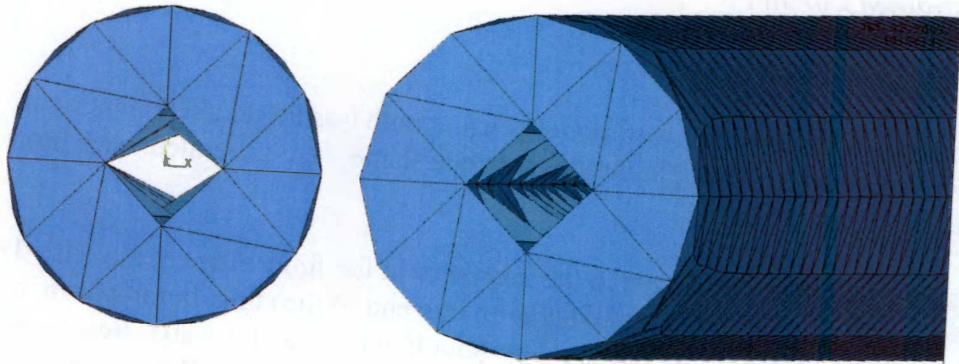


Figure 28: Tet Mesh 1

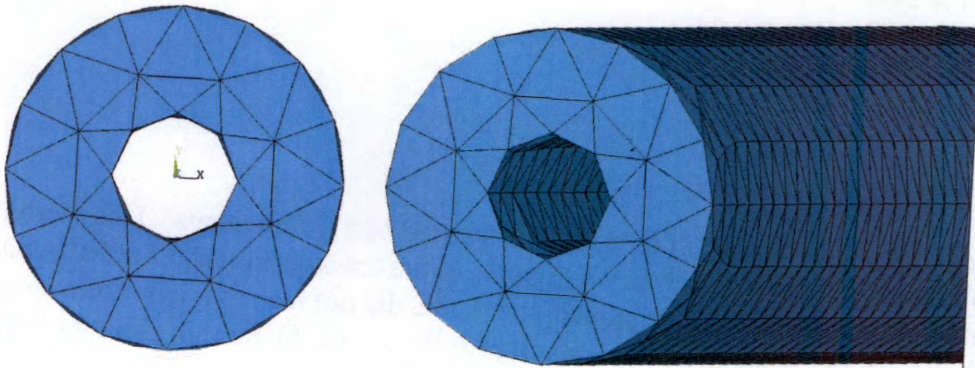


Figure 29: Tet Mesh 2

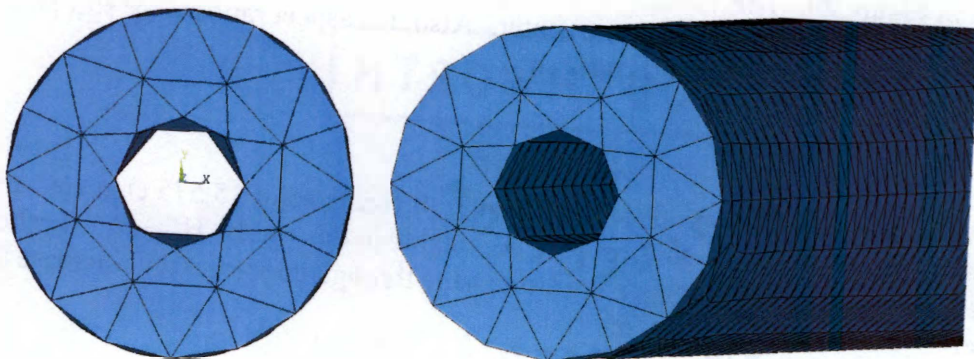


Figure 30: Tet Mesh 3

Tet Mesh 4

Tet Mesh 3 was refined to produce Tet Mesh 4. It consisted of 97,776 elements and can be seen in Figure 31. This was an acceptable mesh, and no further refinement was desired.

Quadrilateral Meshes

The quadrilateral meshes for the sting only configuration can be seen in Figures 32-34.

Quad Mesh 1

The initial quadrilateral mesh (Quad Mesh 1) consisted of 3840 elements. It can be seen in Figure 32. This mesh was very course in the cross section and needed refinement. Also, the default settings of the automatic meshing feature in ANSYS created too many elements with poor aspect ratios.

Quad Mesh 2

Quad Mesh 1 was refined to produce Quad Mesh 2. It contained 125,008 elements and can be seen in Figure 33. This mesh contained a satisfactory number of elements in the cross section, but it still had poor aspect ratios. Therefore, further refinement was needed.

Quad Mesh 3

Quad Mesh 2 was refined to produce Quad Mesh 3. It contained 20,176 elements and can be seen in Figure 34. This was an acceptable mesh, and no further refinement was desired.

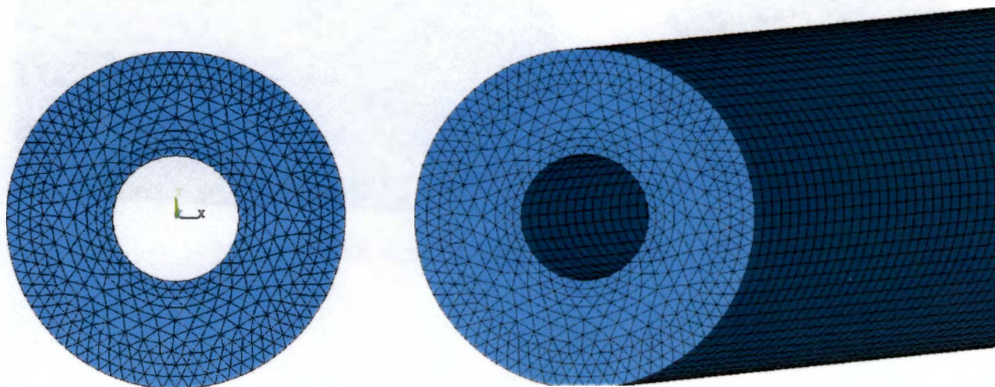


Figure 31: Tet Mesh 4

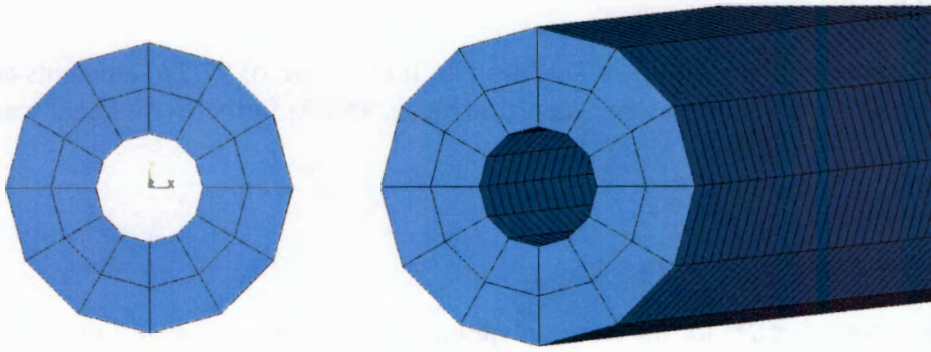


Figure 32: Quad Mesh 1

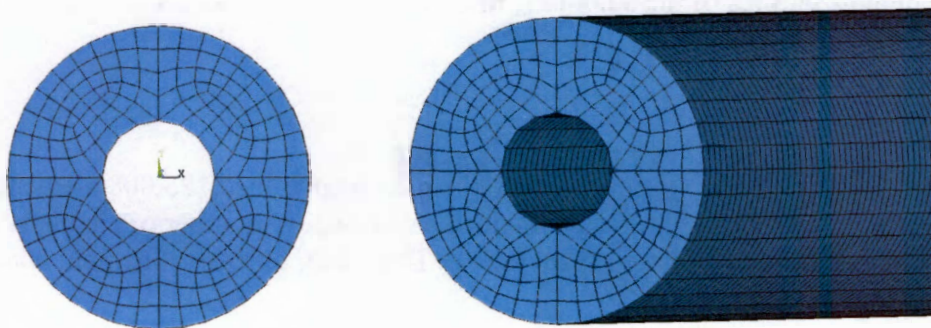


Figure 33: Quad Mesh 2

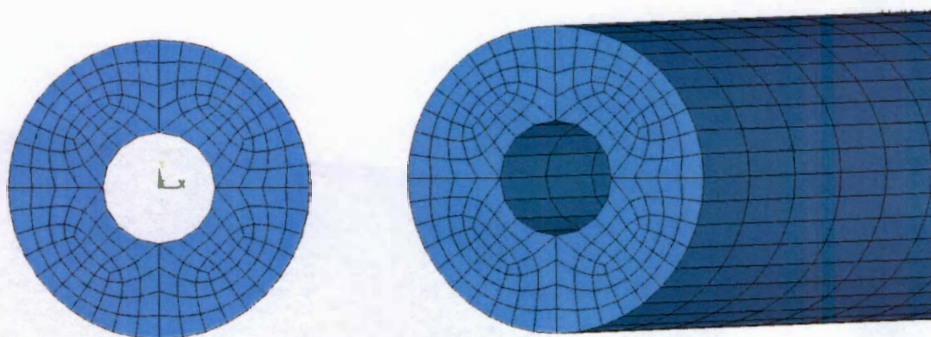


Figure 34: Quad Mesh 3

Sting + Nut Configuration

The sting plus nut configuration was modeled using tetrahedron elements. The automatic meshing tool was used to generate the grid. This mesh consisted of 461,605 elements and can be seen in Figure 35. Ideally, there should be a greater number of elements in the high stress region. However, only one mesh was generated for this configuration because it was satisfactory; an adequate number of elements existed throughout the model.

As in the sting only configuration, some simplifications were made to the geometry in the finite element model. The sting was again modeled as a uniform cylinder with a constant inner radius, and the threading on the nut was modeled as a smooth surface. These things, however, should not introduce a significant amount of error into the results.

Sting + Nut + Balance and Calibration Device Configuration

The configuration consisting of the sting, nut, and balance and calibration device was modeled using both quadrilateral and tetrahedron elements. The automatic meshing tool was used to generate the grid. This mesh consisted of 41,147 elements, and it can be seen in Figure 36. As in the sting plus nut configuration, there would ideally be a greater number of elements in the high stress region. However, only one mesh was generated for this configuration because it was satisfactory; an adequate number of elements existed throughout the model.

As in the previous configurations, some simplifications were made to the geometry in this finite element model. The sting was again modeled as a uniform cylinder with a constant inner radius. Also, the plates on the calibration device were modeled as solid plates, rather than as plates with small holes to be used to adjust the mass distribution during calibration. A picture of the actual balance and calibration device can be seen in Figure 12.

Constrained Condition

All of the meshes in this section were generated by adding constraints to the end of the sting in the acceptable meshes for the unconstrained condition. Constraints were added in all three directions to every node on the end of the sting. Therefore, the number of elements and all the properties remain the same for each mesh. The constrained meshes for all three configurations can be seen in Figures 37 – 42.

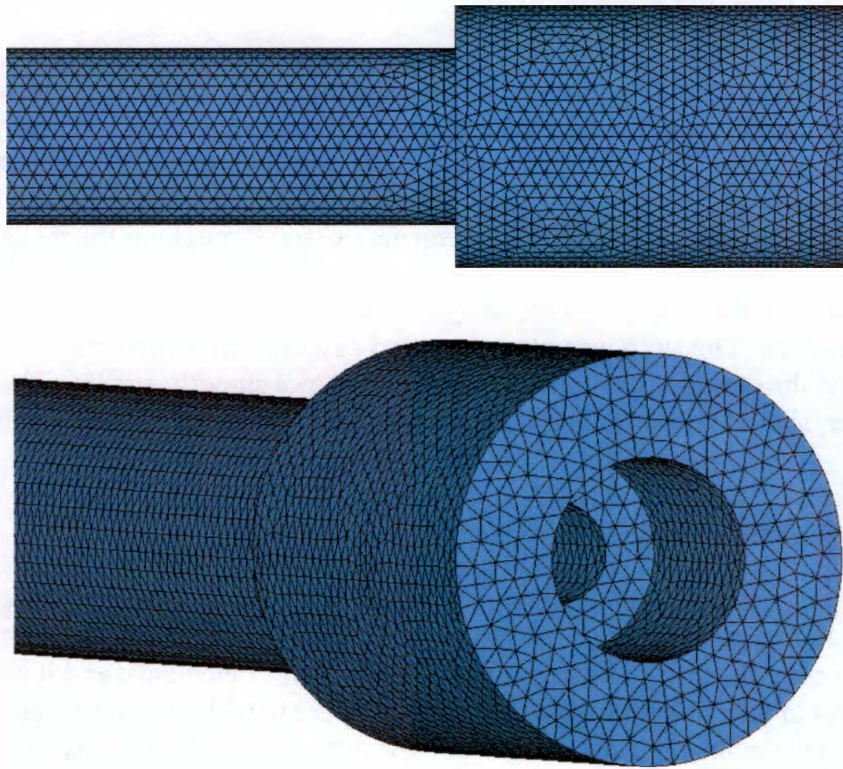


Figure 35: Sting + Nut Configuration – Finite Element Model

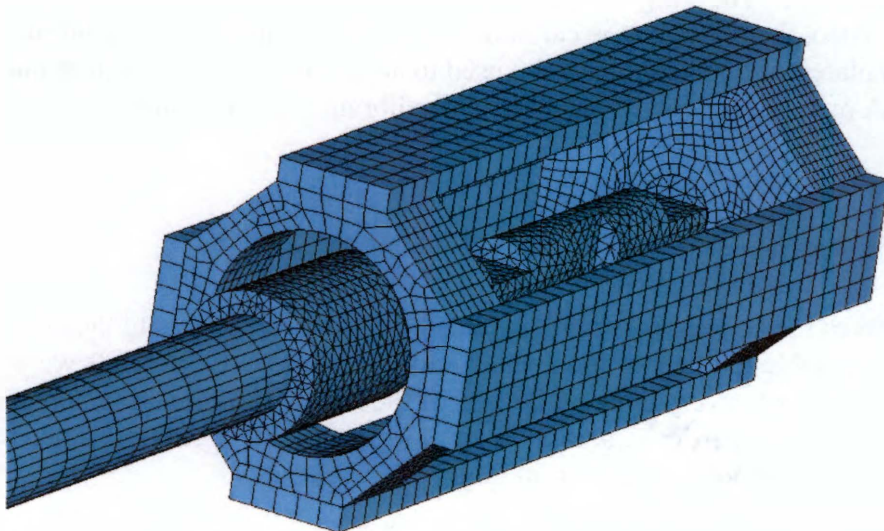


Figure 36: Sting + Nut + Balance and Calibration Device Configuration – Finite Element Model

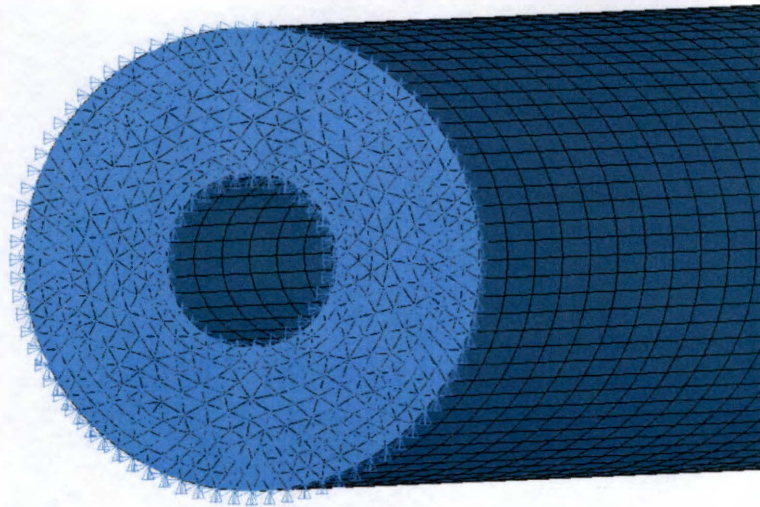


Figure 37: Sting Only Tetrahedron Mesh for Constrained Condition – View 1



Figure 38: Sting Only Tetrahedron Mesh for Constrained Condition – View 2

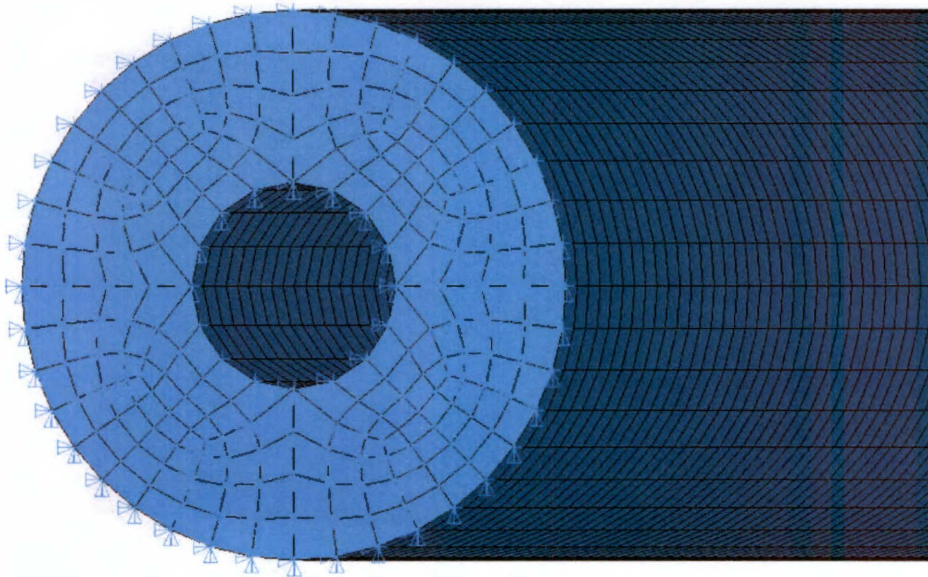


Figure 39: Sting Only Quadrilateral Mesh for Constrained Condition – View 1

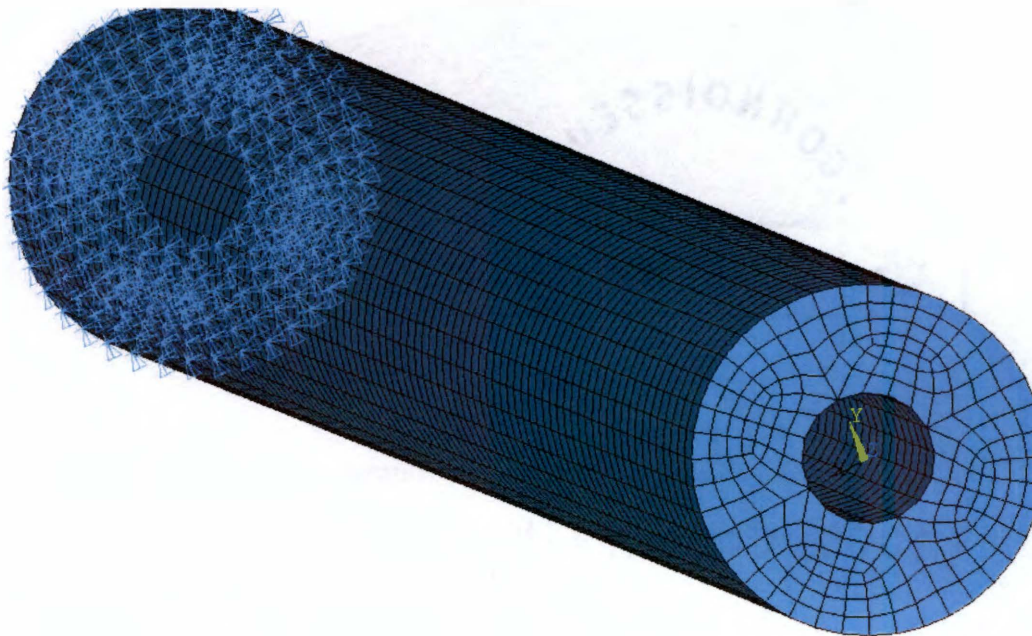


Figure 40: Sting Only Quadrilateral Mesh for Constrained Condition – View 2

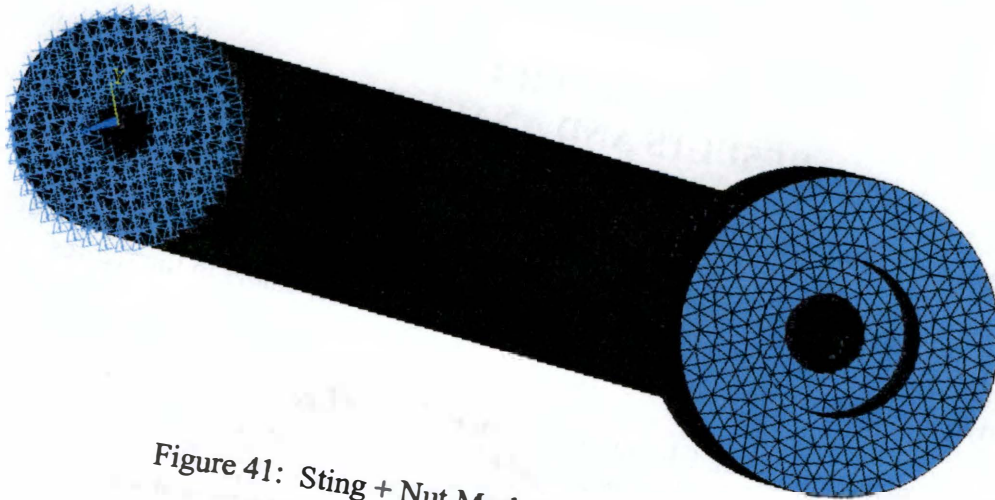


Figure 41: Sting + Nut Mesh for Constrained Condition

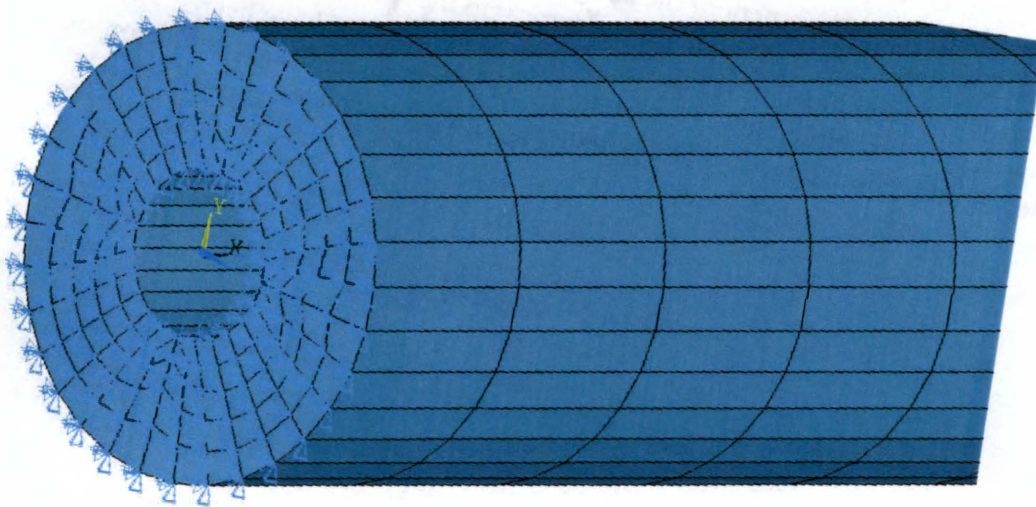


Figure 42: Sting + Nut + Balance and Calibration Device Mesh for Constrained Condition – Constrained End Only

CHAPTER 4 RESULTS AND ANALYSIS

Shaker Table Experiment Without Damping

The data collected was plotted in Excel to determine the natural frequencies of the model. These graphs are shown in Figures 43, 44, and 45. The different colors in the figures correspond to the different accelerometers

As can be seen in Figures 43 and 44 below, this model has a frequency peak at approximately 11 Hz, as expected. The plot in Figure 45 does not show the low range peak because the shaker table was set up to begin the frequency sweep for this run at 10 Hz, and it was unable to register the peak. Subsequent runs were begun at a frequency of 7 Hz.

Possible sources of error introduced into the results include the following:

- It is likely that the attachment of the sting to the shaker table (the clamp) was not completely rigid, thus introducing some error into the results.
- The accelerometer installed on the calibration body may not have been completely on the end block. Part of it may have been in contact with the top plate, thereby allowing it to pick up frequencies from the plate.

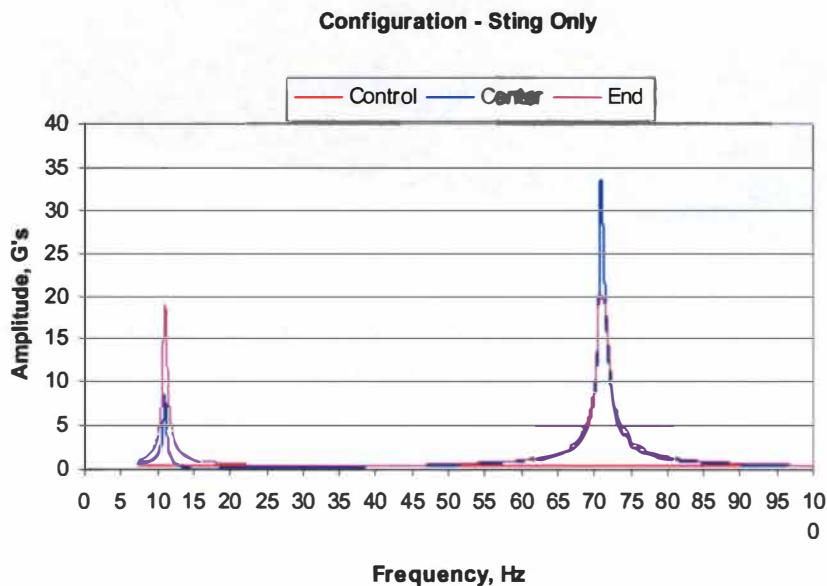


Figure 43: Frequency Plot of Sting Only Configuration

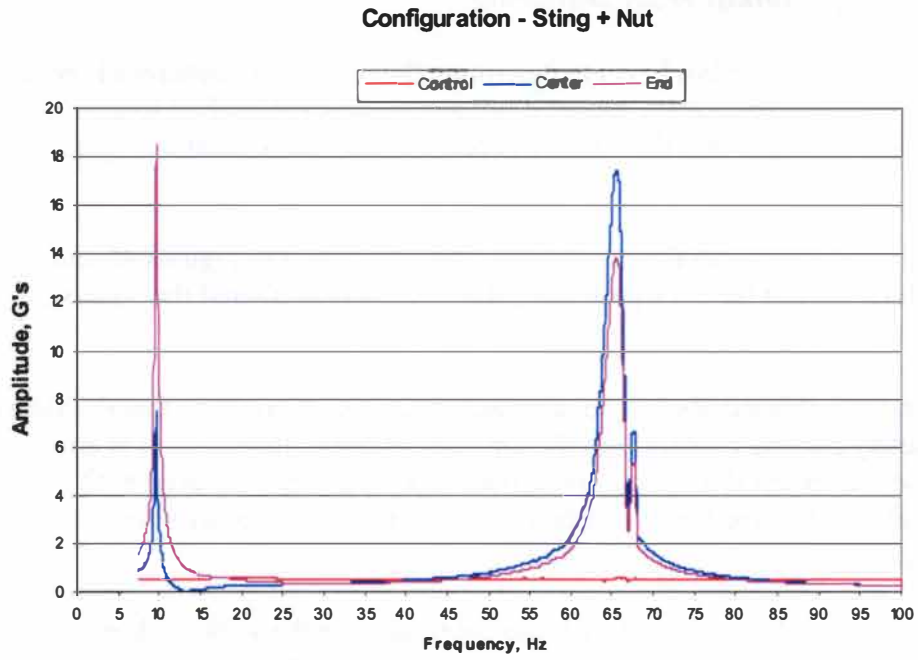


Figure 44: Frequency Plot of the Sting + Nut Configuration

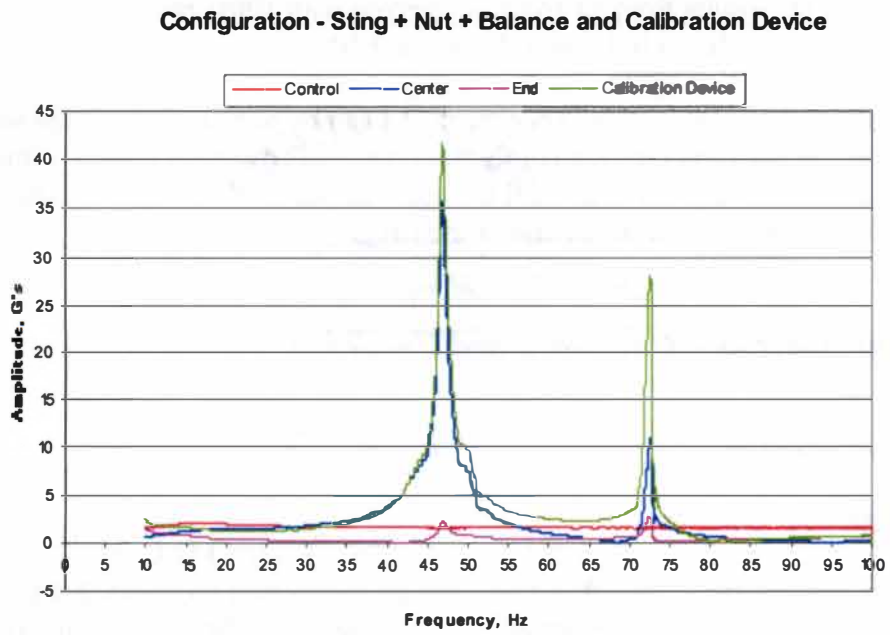


Figure 45: Frequency Plot of Sting + Nut + Balance Configuration

Shaker Table Experiment With Damping

The data collected was plotted in Excel to determine the natural frequencies of the model. Since the low frequency range is the range of interest, results for the first frequency peak from the sting accelerometer and the balance accelerometer can be seen in Figures 46 and 47.

These results did not agree with the expected results. As shown in Figures 46 and 47, the sleeve and v-block did not have a significant effect. They only altered the results approximately ± 1.2 Hz.

There are several possible causes for the unexpected results. It could be that the sleeve was not completely making contact with the top and bottom of the sting. It is also possible that the aluminum sleeve was not stiff enough; therefore, it flexed with the sting. Another possibility is that the lengths were too short for to significantly alter the frequency response.

Other possible sources of error introduced into the results are the same as those mentioned in the shaker table experiment without damping section.

Impulse Testing Experiment

The data obtained in this experiment was plotted in Excel to determine the natural frequencies of the model with an unconstrained boundary condition. For each of the three configurations, the results from all five trials agreed with 100% precision. One plot from each configuration is shown in Figures 48, 49, and 50.

Table 3 summarizes the results for this experiment. As can be seen in Table 3, the sting only configuration and the sting plus nut configuration produced similar results. This was expected because the sting is so long and the nut is so small. This indicates that the nut acts only as an additional mass at the end of the sting.

Finite Element Analysis – Unconstrained Condition

Sting – Only Configuration

Tetrahedron Meshes

As can be seen in Table 4, the solutions did not vary greatly, which indicates that the number of elements is not a significant factor in modal analysis. The results from Tet Mesh 4, the one chosen as acceptable, differ by almost 25% from the Impulse Testing results. A small portion of this difference is due to the fact that some simplifications were made to the geometry in the finite element model as previously discussed.

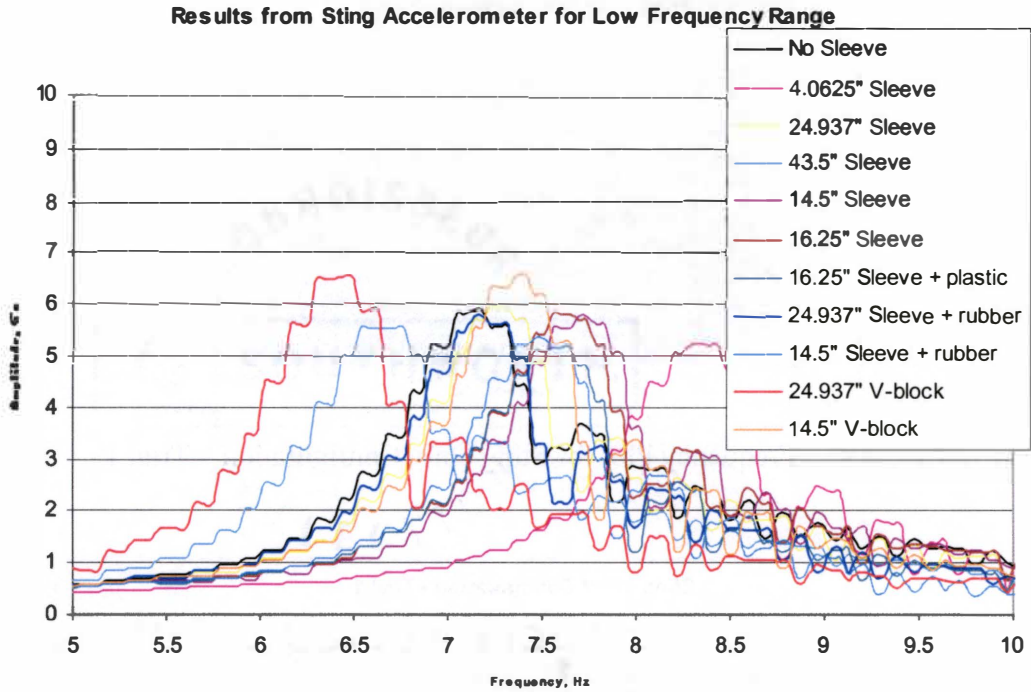


Figure 46: Results from Sting Accelerometer for Low Frequency Range

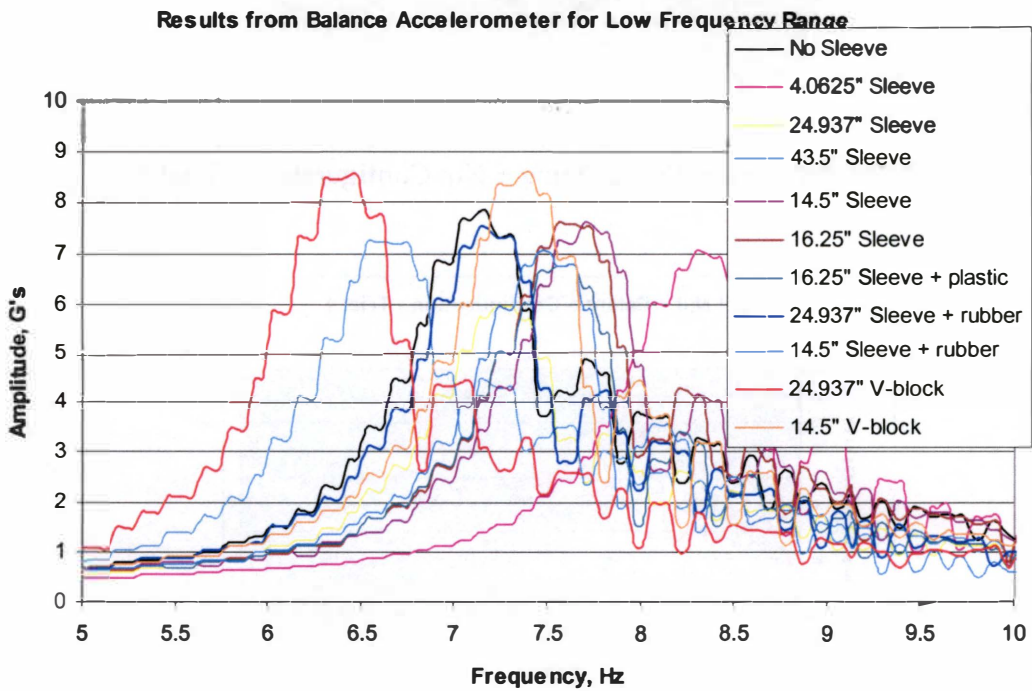


Figure 47: Results from Balance Accelerometer for Low Frequency Range

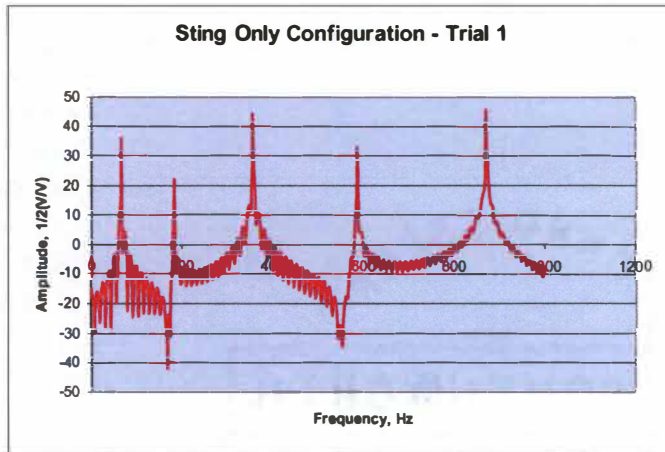


Figure 48: Frequency Plot for Sting Only Configuration – Trial 1

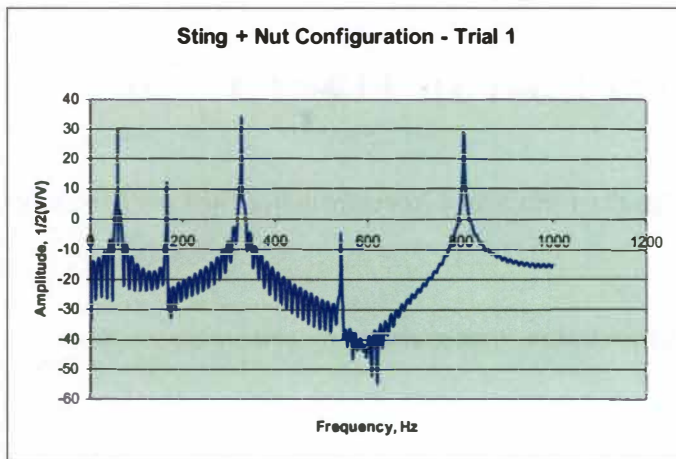


Figure 49: Frequency Plot for Sting + Nut Configuration – Trial 1

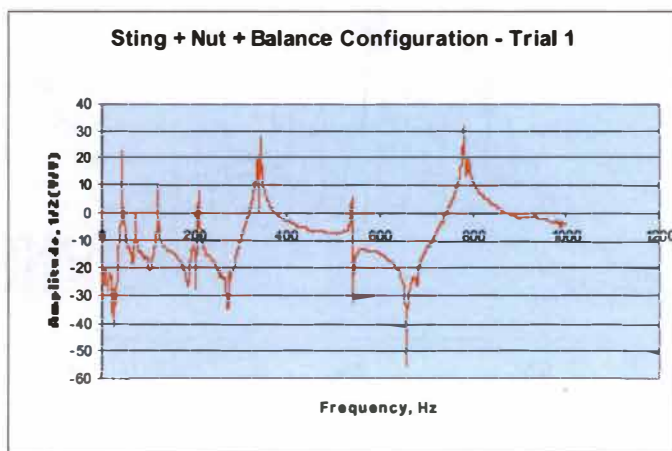


Figure 50: Frequency Plot for Sting + Nut + Balance Configuration – Trial 1

Table 3: Results Summary for Impulse Testing Experiment

	Sting Only	Sting + Nut	Sting + Nut + Balance & Calibration Device
Peak 1	66.25	59.375	43.75
Peak 2	182.5	165.625	73.125
Peak 3	355.625	326.25	120.625
Peak 4	586.25	540.625	208.75
Peak 5	870	806.875	343.75

*Units are in Hz.

Table 4: Results Summary for Tetrahedron Meshes

	Impulse Testing Results	Tet Mesh 1	% Diff.	Tet Mesh 2	% Diff.	Tet Mesh 3	% Diff.	Tet Mesh 4	% Diff.
Peak 1	66.25	86.153	30.04%	82.598	24.68%	85.695	29.35%	82.664	24.78%
Peak 2	182.5	236.97	29.85%	227.1	24.44%	235	28.77%	227.35	24.58%
Peak 3	355.625	462.84	30.15%	443.64	24.75%	458.44	28.91%	444.21	24.91%
Peak 4	586.25	760.42	29.71%	729.82	24.49%	755.77	28.92%	731.09	24.71%
Peak 5	870	1130.9	29.99%	1083.5	24.54%	1124.9	29.30%	1086.3	24.86%

*Units are in Hertz.

One simplification that did have a significant effect was the length of the sting (modeled as 48 in. rather than 51.33 in.). A portion of this difference also likely comes from error that was probably introduced in the Impulse Testing experiment. In addition, the aspect ratio was not perfect. Therefore, even though there is a sizable difference in the results from the experiment and Tet Mesh 4, Tet Mesh 4 was chosen as the best mesh because it has a good grid throughout the model.

Quadrilateral Meshes

As can be seen in Table 5, the solutions did not vary greatly, which indicates that the number of elements is not a significant factor in modal analysis. The results from the acceptable mesh, Quad Mesh 3, differ from the Impulse Testing results by about 22%. The reasons for this difference are similar to the reasons for the difference in the Tetrahedron mesh results. Therefore, even though there is a significant difference in the results from the experiment and Quad Mesh 3, Quad Mesh 3 was chosen as the best mesh because it has a good grid throughout the model.

Sting + Nut Configuration

As seen in Table 6, a 10% - 15% difference exists between the results from the experiment and the finite element model. A portion of this error comes from simplifications made in the geometry as well as error that was probably introduced in the

Table 5: Results Summary for Quadrilateral Meshes

	Impulse Testing Results	Quad Mesh		Quad Mesh		Quad Mesh	
		1	% Diff.	2	% Diff.	3	% Diff.
Peak 1	66.25	79.422	19.88%	80.917	22.14%	80.955	22.20%
Peak 2	182.5	218.39	19.67%	222.44	21.88%	222.66	22.01%
Peak 3	355.625	426.61	19.96%	434.34	22.13%	435.08	22.34%
Peak 4	586.25	701.88	19.72%	714.2	21.83%	716.14	22.16%
Peak 5	870	1042.4	19.82%	1060	21.84%	1064.2	22.32%

*Units are in Hz.

Table 6: Results from the Sting + Nut Configuration

	Impulse Testing Results	Sting+Nut Mesh	% Diff.
Peak 1	59.375	73.045	10.26%
Peak 2	165.625	204.48	12.04%
Peak 3	326.25	404.27	13.68%
Peak 4	540.625	670.67	14.40%
Peak 5	806.875	1001.7	15.14%

*Units are in Hertz.

Impulse Testing experiment. In addition, the aspect ratio was not perfect. Therefore, since the mesh and geometry look good throughout the model, the mesh was considered satisfactory.

Sting + Nut + Balance and Calibration Device Configuration

As seen in Table 7, the difference that exists between the results from the experiment and the finite element model varies greatly from one mode to another. A significant portion of this error likely comes from the simplifications described previously. Also, a portion of it is due to error that was probably introduced in the Impulse Testing experiment. One additional source of error is that it appeared that the grids were possibly not connected in several locations. In addition, the aspect ratio was not perfect. Therefore, since the mesh and geometry look good throughout the model, the mesh was considered satisfactory.

Finite Element Analysis – Constrained Condition

Sting-Only Configuration

As was discussed in the introduction of this paper, these models should have mode shapes similar to those shown in Figure 8. Figures 51-56 show the mode shapes for the first three fundamental frequencies of the sting, and they resemble those in Figure 8 as expected. (Figures 51-53 are the mode shapes for the tetrahedron meshes, and Figures 54-56 are the mode shapes for the quadrilateral meshes.) The deflections in these figures, as in the mode shape figures throughout the rest of this paper, are greatly exaggerated. The results from the solutions for the tetrahedron and quadrilateral meshes can be seen in Table 8.

Table 7: Results from the Sting + Nut + Balance and Calibration Device Configuration

	Impulse Testing Results	Sting+Nut+Balance & Calibration Device Mesh	% Diff.
Peak 1	43.75	43.645	0.24%
Peak 2	73.125	57.111	21.90%
Peak 3	120.625	111.86	7.27%
Peak 4	209.375	205.14	2.02%
Peak 5	343.75	313.22	8.88%

*Units are in Hertz.

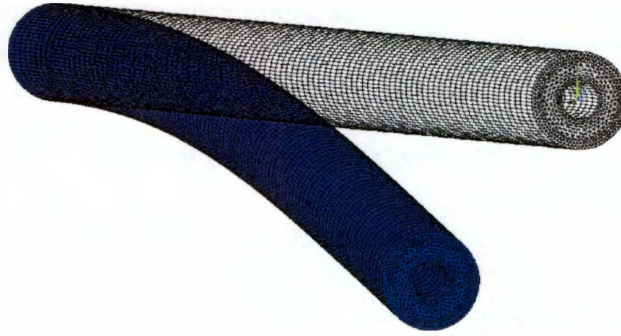


Figure 51: Sting Only Tetrahedron Mesh for Constrained Condition – Plot of 1st Mode Shape (distorted)

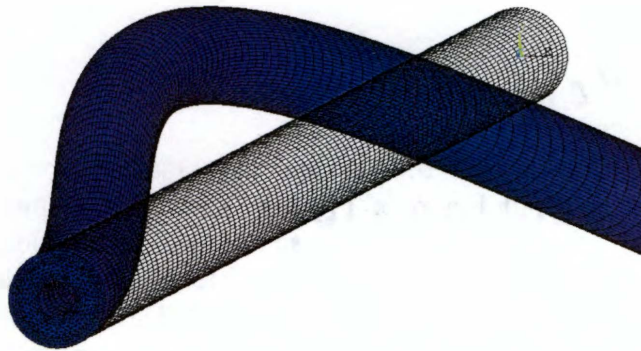


Figure 52: Sting Only Tetrahedron Mesh for Constrained Condition – Plot of 2nd Mode Shape (distorted)

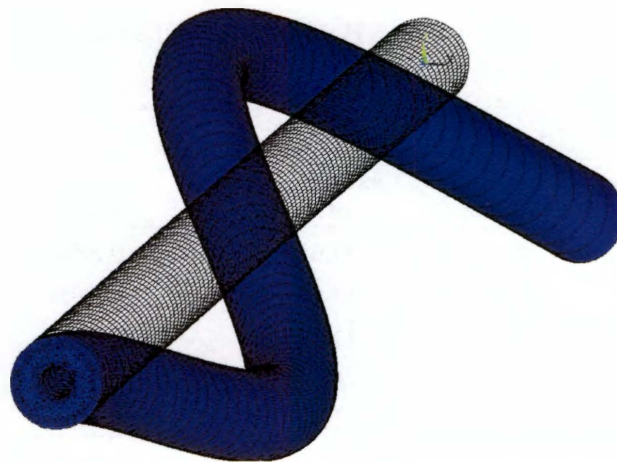


Figure 53: Sting Only Tetrahedron Mesh for Constrained Condition – Plot of 3rd Mode Shape (distorted)

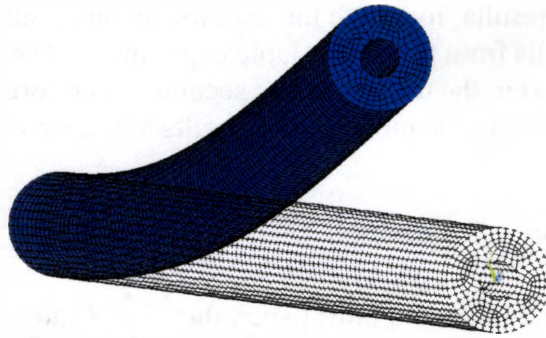


Figure 54: Sting Only Quadrilateral Mesh for Constrained Condition – Plot of 1st Mode Shape (distorted)

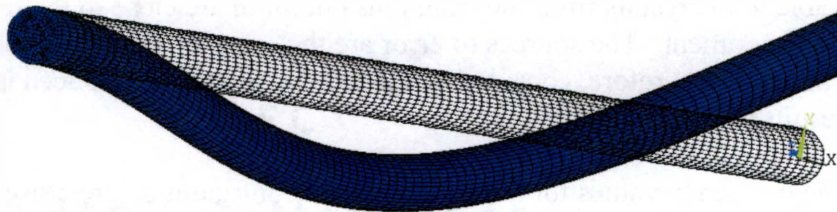


Figure 55: Sting Only Quadrilateral Mesh for Constrained Condition – Plot of 2nd Mode Shape (distorted)

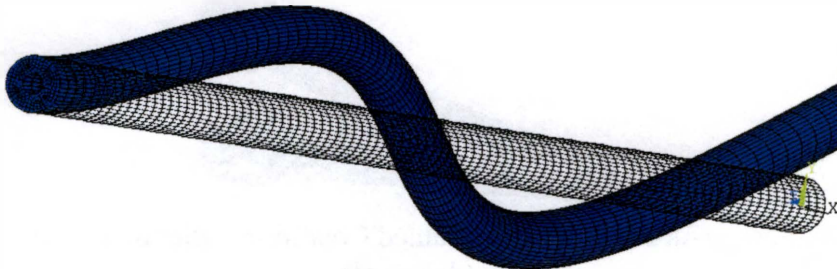


Figure 56: Sting Only Quadrilateral Mesh for Constrained Condition – Plot of 3rd Mode Shape (distorted)

Table 8: Results Summary for Sting Only Meshes – Constrained Condition

	Shaker Table	Tetrahedron Mesh	% Difference	Quadrilateral Mesh	% Difference
Peak 1	11.025	13.027	18.20%	12.757	15.70%
Peak 2	70.944	81.493	14.90%	79.807	12.50%

*Units are in Hz.

As shown in Table 8, the results from both the tetrahedron mesh and the quadrilateral mesh are close to the results from the shaker table experiment. The sources of error are the same as those described in the unconstrained section. Therefore, considering the sources of error introduced into the model, these results are acceptable.

Sting + Nut Configuration

As was discussed in the introduction of this paper, this model should have mode shapes similar to those shown in Figure 8. Figures 57, 58, and 59 show the mode shapes for the first three frequencies of the sting plus nut configuration, and they resemble those in Figure 8 as expected. The results from the solution for this mesh can be seen in Table 9 below.

As shown in Table 9, the results from the sting plus nut mesh are close to the results from the shaker table experiment. The sources of error are the same as those described in the unconstrained section. Therefore, considering the sources of error introduced into the model, these results are acceptable.

As expected, the frequency values for the sting plus nut configuration are close to those of the sting only configuration. This is because the sting is so long, and the nut is so small. Therefore, the nut is not a critical component of the frequency.



Figure 57: Sting + Nut Mesh for Constrained Condition – Plot of 1st Mode Shape (distorted)



Figure 58: Sting + Nut Mesh for Constrained Condition – Plot of 2nd Mode Shape (distorted)

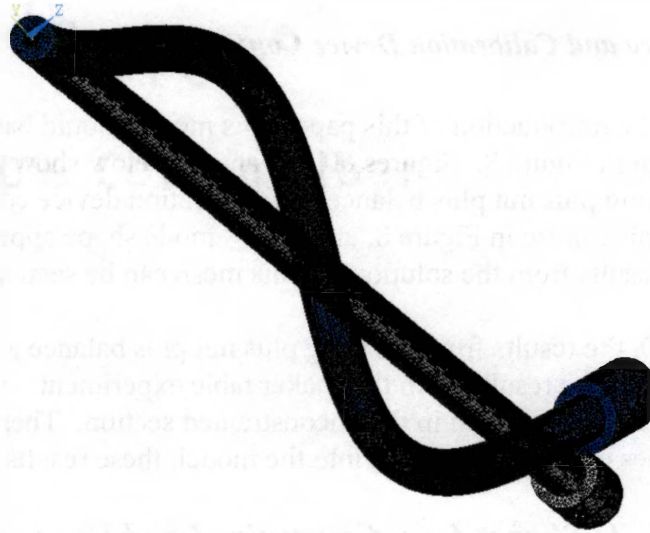


Figure 59: Sting + Nut Mesh for Constrained Condition – Plot of 3rd Mode Shape (distorted)

Table 9: Results Summary for Sting + Nut Mesh – Constrained Condition

	Shaker Table	Sting+Nut Model	% Difference
Peak 1	9.669	11.202	15.9
Peak 2	65.612	72.02	9.8

*Units are in Hertz.

Sting + Nut + Balance and Calibration Device Configuration

As was discussed in the introduction of this paper, this model should have mode shapes similar to those shown in Figure 8. Figures 60, 61, and 62 below show the first three mode shapes of the sting plus nut plus balance and calibration device configuration. The first two modes resemble those in Figure 8, and the 3rd mode shape appears to be a balance mode. The results from the solution for this mesh can be seen in Table 10.

As shown in Table 10, the results from the sting plus nut plus balance and calibration device mesh are close to the results from the shaker table experiment. The sources of error are the same as those described in the unconstrained section. Therefore, considering the sources of error introduced into the model, these results are acceptable.

Comparison of Mode Shapes from Constrained and Unconstrained Condition

The mode shapes for each of the three configurations (sting only, sting plus nut, and sting plus nut plus balance and calibration device) were similar in both the constrained and unconstrained conditions. In each case, the constrained condition had one extra mode shape. To demonstrate this information, a complete list of results and the mode shape images for the sting plus nut plus balance and calibration device configuration will be included below in Table 11 and Figures 63-71. The correspondence between the results and mode shapes for the other two configurations is similar. Tables E-1, E-2, and E-3 in Appendix E compare the results for the sting only and sting plus nut configurations.

In Table 11, the letters correspond to the different mode shapes. The numbers correspond to the vertical and horizontal directions. For example, A1 and A2 correspond to the vertical and horizontal directions of the first mode shape. Ansys solved for both directions, where applicable, in all solutions, but only one direction was measured in the experiments.

In Table 11, the first mode shape for the constrained condition, Rows A1 and A2, is similar to Mode 1 in Figure 8 in the first section of this paper. The experimental result for this mode is unknown because the start frequency in the shaker table experiment was too high. This mode shape does not appear in the unconstrained condition because it is not constrained in such a way as to allow vibration in this mode. Row B corresponds to the 2nd mode shape for the constrained condition and the 1st mode shape for the unconstrained condition, respectively. These mode shapes are similar to the mode shapes in Figure 8. Rows C1 and C2 correspond to the 3rd mode shape for the constrained condition and the 2nd mode shape for the unconstrained condition, respectively. Row D is an unknown mode. Rows E1 and E2 correspond to the 4th mode shape for the constrained condition and the 3rd mode shape for the unconstrained condition, respectively. Rows F1 and F2 correspond to the 5th mode shape for the constrained condition and the 4th mode shape for the unconstrained condition, respectively.



Figure 60: Sting + Nut + Balance and Calibration Device Mesh for Constrained Condition Plot of 1st Mode Shape (distorted)



Figure 61: Sting + Nut + Balance and Calibration Device Mesh for Constrained Condition Plot of 2nd Mode Shape (distorted)

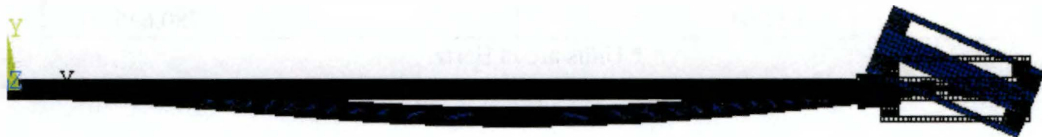


Figure 62: Sting + Nut + Balance and Calibration Device Mesh for Constrained Condition Plot of 3rd Mode Shape (distorted)

Table 10: Results Summary for Sting + Nut + Balance and Calibration Device Mesh – Constrained Condition

	Sting+Nut+Balance and Calibration		
	Shaker Table	Device Model	% Difference
Peak 1	unknown	7.81	unknown
Peak 2	46.89	43.12	8.04
Peak 3	72.65	57.09	21.4

* Units are in Hertz

Table 11: Results comparison for Sting + Nut + Balance and Calibration Device Configuration

	Computational Results - Constrained Condition	Experimental Results - Constrained Condition	Computational Results - Unconstrained Condition	Experimental Results - Unconstrained Condition
A1	5.5278	unknown		
A2	7.8101			
B	43.12	46.89	43.645	43.75
C1	57.086	72.65	57.111	73.125
C2	57.326		57.325	
D	85.91			
E1	111.67		111.86	120.625
E1	135.57		135.52	
F1	205.32		205.14	209.375
F2	247.58		247.48	
	395.75		313.22	343.75
	419.45			538.75
	540			
	655.04			

* Units are in Hertz.



Figure 63: 1st Mode Shape for Constrained Condition (distorted)



Figure 64: 2nd Mode Shape for Constrained Condition (distorted)



Figure 65: 1st Mode Shape for Unconstrained Condition (distorted)



Figure 66: 3rd Mode Shape for Constrained Condition (distorted)



Figure 67: 2nd Mode Shape for Unconstrained Condition (distorted)



Figure 68: 4th Mode Shape for Constrained Condition (distorted)



Figure 69: 3rd Mode Shape for Unconstrained Condition (distorted)



Figure 70: 5th Mode Shape for Constrained Condition (distorted)



Figure 71: 4th Mode Shape for Unconstrained Condition (distorted)

CHAPTER 5

CONCLUSIONS AND RECOMMENDATIONS

Wind tunnel sting being modeled and studied in this thesis has a typically low natural frequency, in the range of 8 Hz to 14 Hz. Therefore, since the model used in the shaker table experiment with no damping had a natural frequency in the same range (approximately 11 Hz), this experiment proved that this model represented to the wind tunnel sting.

The sleeve used for attenuation and damping of the natural vibration modes had a definite effect in the shaker table experiment with damping; however, this effect on measured first mode frequencies was smaller than expected. The frequency response varied depending on the location of the sleeve. Thus, it was an effective way to attenuate the frequency. With some modifications to the sleeve design, it is expected that the sleeve would have a greater effect on the frequency.

Based on the results from the shaker table experiment with damping, the sleeve appears to have more of a stiffening effect when it is placed near the clamped end because the frequency of the first mode increases. This is due to the fact that the sting would bend the most in this area. However, when it is placed at the other end near the balance, the sleeve's mass affects the frequency more than its stiffening characteristics. This is evident since the frequency is lower, due to the fact that it takes more energy to vibrate the sting with more weight near the end.

The finite element analysis results were reasonably close to the experimental results for each condition and configuration modeled, considering the modeling simplifications. Therefore, based on assumptions applied in the use of this code, it can be concluded that the difference with the experimental results is acceptable.

The following recommendations are suggested in an effort to improve the results from the shaker table experiment with damping.

1. Fabricate a new sleeve made from a stiffer material, perhaps carbon steel.
2. Conduct further tests using damping material such as plastic or rubber between the sleeve and the sting to see what effect they have on the results.
3. Vary the weight of the sleeve by changing the thickness to evaluate the weight effect on the results.

BIBLIOGRAPHY

- [1] Fehren, H., Gnauert, U., and Wimmel, R., "Validation Testing with the Active Damping System in the European Transonic Windtunnel," AIAA 2001-0610, 39th AIAA Aerospace Sciences Meeting and Exhibit, Reno, Nevada, January 8-11, 2001.
- [2] Buehrle, R. D., Young, C. P., Balakrishna, S., and Kilgore, W. A., "Experimental Study of Dynamic Interaction Between Model Support Structure and a High Speed Research Model in the National Transonic Facility," AIAA-94-162.
- [3] Cole, S. R. and Henning, T. L., "Buffet Response of a Hammerhead Launch Vehicle Wind-Tunnel Model," AIAA-91-1050, 32nd AIAA/ASME/ASCE/AHS/ASC Structures, Structural Dynamics, and Materials Conference, Baltimore, Maryland, April 8-10, 1991.
- [4] Tzou, H. S. and Tseng, C. I., "Distributed Piezoelectric Sensor/Actuator Design for Dynamic Measurement/Control of Distributed Parameter Systems: A Piezoelectric Finite Element Approach," *Journal of Sound and Vibration*, Vol. 138, No. 1, April 1989, pp. 17-34.
- [5] Moses, R. W., Wieseman, C. D., Bent, A. A., and Pizzochero, A. E., "Evaluation of New Actuators in a Buffet Loads Environment," *Proceedings of SPIE—The International Society for Optical Engineering*, Vol. 4332, 2001.
- [6] De Silva, C. W., "Vibration: Fundamentals and Practice," ISBN 0-8493-1808-4.
- [7] ANSYS 7.0 Help Documentation.
- [8] Azvine, B., Wynne, T. J., and Tomlinson, G. R., "Active Damping for the Control of Flexible Structures," International Conference on Control (University of Warwick), Vol. 2, No. 389, 1994, pp. 1296-1305.
- [9] Buravalla, V. R., Bhattacharya, B., and Tomlinson, G. R., "Hybrid Vibration Control of Laminated Composite Structures Using Magnetostrictive and Hard Damping Materials," *Proceedings of SPIE – The International Society for Optical Engineering*, Vol. 4331, 2001, pp. 386-395.
- [10] Ewald, B. F. R., "Multi-Component Force Balances for Conventional and Cryogenic Wind Tunnels," *Measurement Science and Technology*, Vol. 11, No. 6, 2000, pp. R81-R94.
- [11] Ferro, A. A. and Heck, B. S., "Analytical Investigation of Damping Enhancement Using Active and Passive Structural Joints," *Journal of Guidance, Control, and Dynamics*, Vol. 15, No. 5, September-October 1992, pp. 1258-1264.

- [12] Heeg, J., McGowan, A., Crawley, E., and Lin, C., "The Piezoelectric Aeroelastic Response Tailoring Investigation: A Status Report," *Proceedings of SPIE – The International Society for Optical Engineering*, Vol. 2447, 1995, pp. 2-13.
- [13] Li, J. and Xiong, S., "Experimental Studies of Vibration Control of a Space Truss Structure," *Proceedings of the 16th International Modal Analysis Conference*, Vol. 1, 1998, pp. 263-269.
- [14] McDevitt, T. K. and Owen, F. K., "An Optical Angle of Attack Sensor," *IEEE Aerospace and Electronic Systems Magazine*, Vol. 5, No. 2, February 1990, pp. 19-27.
- [15] McGowan, A. R. and Lake, R. C., "Results of Wind-Tunnel Testing from the Piezoelectric Aeroelastic Response Tailoring Investigation," AIAA-96-1511-CP.
- [16] Moses, R. W., "Vertical Tail Buffeting Alleviation Using Piezoelectric Actuators – Some Results of the Actively Controlled Response of Buffet-Affected Tails (ACROBAT) Program," *Proceedings of SPIE – The International Society for Optical Engineering*, Vol. 3044, 1997, pp. 87-98.
- [17] Preumont, A., Sparavier, M., and Dufour, J., "Application of Piezoelectric Actuators to the Active Damping of a Truss Structure," AIAA-90-0950-CP.
- [18] Su, J. and Chang, T. N., "Enhanced Resolution Michelson Interferometer for Displacement Measurement," *Proceedings of SPIE – The International Society for Optical Engineering*, Vol. 3833, 1999, pp. 133-139.
- [19] Tzou, H. S. and Tseng, C. I., "Distributed Modal Identification and Vibration Control of Continua: Piezoelectric Finite Element Formulation and Analysis," *Journal of Dynamic Systems, Measurement, and Control*, Vol. 113, September 1991, pp. 500-505.
- [20] Uchida, H. and Onoda, J., "Integrated Optimization of Viscoelastic Structures and Active Controllers for Flexible Space Structures," AIAA-2000-1524, 41st AIAA/ASME/ASCE/AHS/ASC Structures, Structural Dynamics, and Materials Conference, Atlanta, Georgia, April 3-6, 2000.
- [21] Vakili, A. D. et. al., "A New Adaptive Technique to Control Vibrations in Cylindrical Devices (Baseball and Softball Bats) and Other Sport Implements." Patent application in progress.
- [22] Wilcox, R. A. and Lockwood, C. T., "Wind Tunnel Balance Behavior."

Appendix A

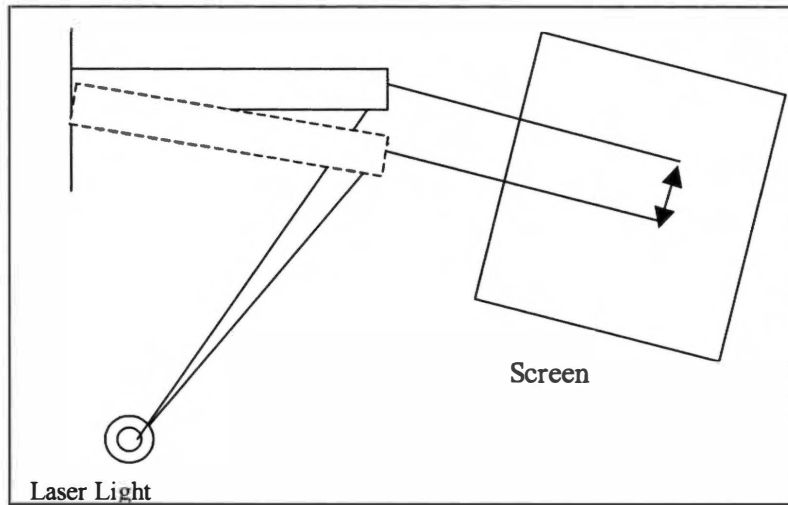


Figure A-1: System for Measuring Deflection with Laser Light Source

A diffuse laser beam is reflected from a point at the end of the sting (cantilever beam) onto a screen, and the amplitude of the vibration is then obtained. This system could be calibrated by manually deflecting the beam one millimeter and then measuring the corresponding deflection on the screen.

Appendix B

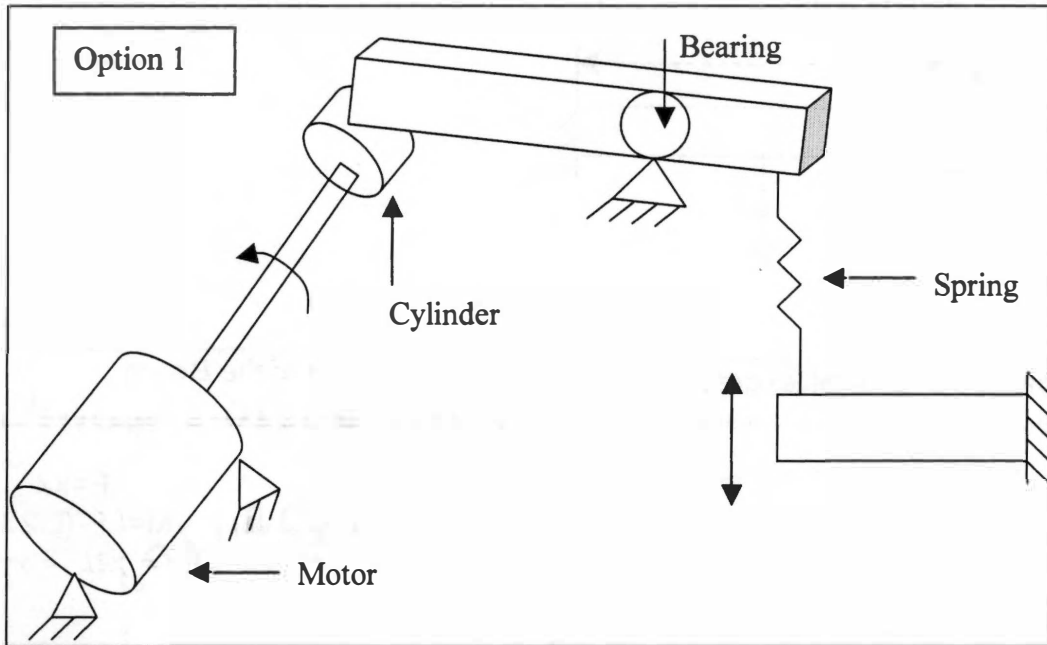


Figure B-1: Option 1 for Producing Deflection in a Beam with a Cell Phone Motor

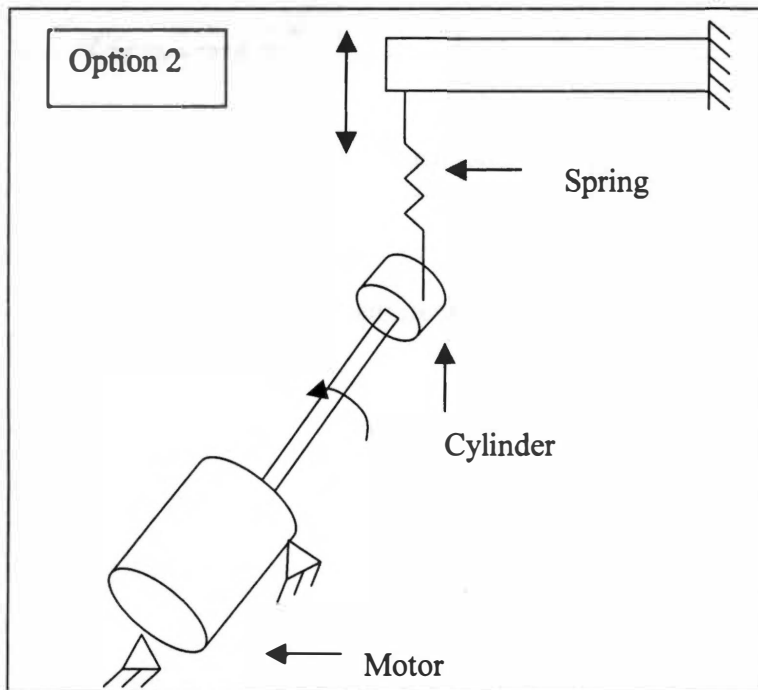
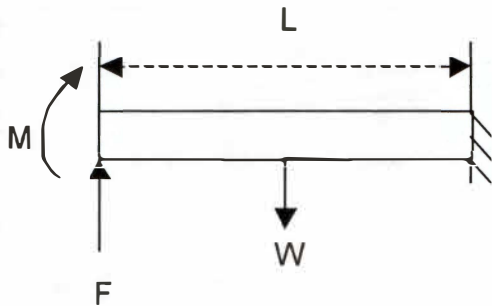


Figure B-2: Option 2 for Producing Deflection in a Beam with a Cell Phone Motor

Appendix C



Vibration of a Cantilevered Beam

Deflection of the Beam

$$\cosh \beta L \cos \beta L + 1 = 0$$

$$\beta^4 = \frac{\gamma A \omega^2}{gEI} \quad \text{where} \quad A = \pi r^2$$

$$\omega = \beta^2 \sqrt{\frac{gEI}{\gamma A}}$$

$$\delta = \left(\frac{L^3}{3EI} \right) F + \left(\frac{L^2}{2EI} \right) M \quad \begin{array}{l} F = kx \\ M = LF - (L/2)W \\ W = \gamma AL = \gamma \pi r^2 L \end{array}$$

$$k = \left[\delta - \left(\frac{L^2}{2EI} \right) M \right] \left(\frac{3EI}{L^3 x} \right)$$

*Let x = delta.

For the fundamental mode of vibration:

$$\beta L \quad 1.875$$

Figure C-1: Calculations for Beam Size

Solid Cylindrical Steel Beam

E (Pa) I (m⁴) G (N/m³)
 2E+11 (pi/4)*r⁴ 77000

where E = Modulus of Elasticity
 I = Area Moment Of Inertia
 G = Specific Weight (gamma)

βL 1.875

L (in)	L (m)	r (in)	r (m)	I (m ⁴)	ω	δ	M (N/m)	k (N/m)	F (N)	F (lbf)	W (N)	W (lbf)
16	0.406	0.3	0.008	2.65E-09	409.17	3	2.32	20816	62.45	14.04	5.71	1.28
16	0.406	0.5	0.013	2.04E-08	681.95	3	6.44	174711	524.13	117.83	15.86	3.56
14	0.356	0.5	0.013	2.04E-08	890.71	3	4.93	265691	797.07	179.19	13.87	3.12
12	0.305	0.25	0.006	1.28E-09	606.18	3	0.91	25571	76.71	17.25	2.97	0.67
10	0.254	0.25	0.006	1.28E-09	872.89	3	0.63	45517	136.55	30.70	2.48	0.56
10	0.254	0.2	0.005	5.23E-10	698.32	3	0.40	18358	55.08	12.38	1.59	0.36
10	0.254	0.2	0.005	5.23E-10	698.32	2	0.40	17962	35.92	8.08	1.59	0.36
10	0.254	0.2	0.005	5.23E-10	698.32	1	0.40	16773	16.77	3.77	1.59	0.36
9	0.229	0.25	0.006	1.28E-09	1077.65	3	0.51	63022	189.07	42.50	2.23	0.50
9	0.229	0.2	0.005	5.23E-10	862.12	3	0.33	25557	76.67	17.24	1.43	0.32
8	0.203	0.25	0.006	1.28E-09	1363.90	3	0.40	90329	270.99	60.92	1.98	0.45
8	0.203	0.2	0.005	5.23E-10	1091.12	3	0.26	36770	110.31	24.80	1.27	0.29

* The motor can produce 10,000 rpm = 1047.2 rad/s.

*Omega is measured in rad/s.
 *Delta is measured in mm.

Figure C-1 Continued

Hollow Cylindrical Steel Beam

E (Pa)		I (m ⁴)		G (N/m ³)		where E = Modulus of Elasticity I = Area Moment Of Inertia G = Specific Weight (gamma)		βL		I (m ⁴) ($\pi/4$)(Ro ⁴ -Ri ⁴)					
2E+11		$(\pi/4)*r^4$		77000				1.875							
L (in)	L (m)	Ro (in)	Ro (m)	Ri (in)	Ri (m)	I (m ⁴)	A (m ²)	ω	δ	M (N/m)	k (N/m)	F (N)	F (lbf)	W (N)	W (lbf)
16	0.406	0.3	0.008	0.25	0.006	1.37E-09	5.57E-05	532.62	3	0.71	12254	36.76	8.26	1.74	0.39
16	0.406	0.3	0.008	0.25	0.006	1.37E-09	5.57E-05	532.62	2	0.71	12254	24.51	5.51	1.74	0.39
16	0.406	0.3	0.008	0.25	0.006	1.37E-09	5.57E-05	532.62	1	0.71	12253	12.25	2.75	1.74	0.39
14	0.356	0.3	0.008	0.25	0.006	1.37E-09	5.57E-05	695.67	3	0.54	18293	54.88	12.34	1.53	0.34
12	0.305	0.3	0.008	0.25	0.006	1.37E-09	5.57E-05	946.88	3	0.40	29049	87.15	19.59	1.31	0.29
10	0.254	0.3	0.008	0.25	0.006	1.37E-09	5.57E-05	1363.50	3	0.28	50196	150.59	33.85	1.09	0.25
9	0.229	0.3	0.008	0.25	0.006	1.37E-09	5.57E-05	1683.34	3	0.22	68857	206.57	46.44	0.98	0.22
8	0.203	0.3	0.008	0.25	0.006	1.37E-09	5.57E-05	2130.48	3	0.18	98040	294.12	66.12	0.87	0.20
22	0.559	0.5	0.013	0.46	0.012	5.79E-09	7.78E-05	490.13	3	1.87	19924	59.77	13.44	3.35	0.75
22	0.559	0.5	0.013	0.45	0.011	7.03E-09	9.63E-05	485.27	3	2.31	24159	72.48	16.29	4.14	0.93
20	0.508	0.5	0.013	0.45	0.011	7.03E-09	9.63E-05	587.18	3	1.91	32157	96.47	21.69	3.77	0.85

* The motor can produce 10,000 rpm = 1047.2 rad/s.

*Omega is measured in rad/s.
*Delta is measured in mm.

Figure C-1 Continued

Hollow Cylindrical Copper Beam

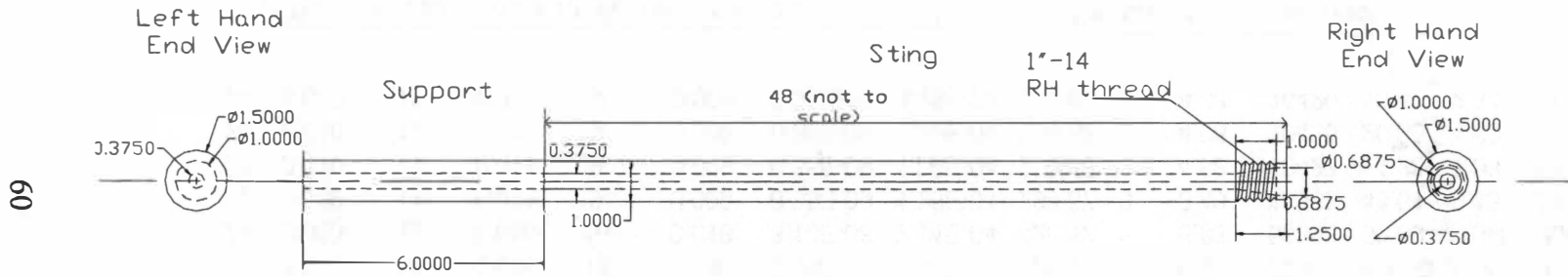
		I (m ⁴)		E (Pa)		G (N/m ³)		βL		1.875						
		(pi/4)(Ro ⁴ -Ri ⁴)		1E+11		87336										
L (in)	L (m)	Ro (mm)	Ro (m)	Ri (mm)	Ri (m)	I (m ⁴)	A (m ²)	ω	δ	M (N/m)	k (N/m)	F (N)	F (lbf)	W (N)	W (lbf)	
18	0.457	14	0.014	13	0.013	7.74E-09	8.48E-05	599.54	3	1.55	30152	90.46	20.34	3.39	0.76	
20	0.508	14	0.014	13	0.013	7.74E-09	8.48E-05	485.63	3	1.91	21980	65.94	14.82	3.76	0.85	
22	0.559	14	0.014	13	0.013	7.74E-09	8.48E-05	401.35	3	2.31	16513	49.54	11.14	4.14	0.93	
24	0.610	14	0.014	13	0.013	7.74E-09	8.48E-05	337.24	3	2.75	12719	38.16	8.58	4.52	1.02	
24	0.610	14	0.014	13	0.013	7.74E-09	8.48E-05	337.24	2	2.75	12718	25.44	5.72	4.52	1.02	
24	0.610	14	0.014	13	0.013	7.74E-09	8.48E-05	337.24	1	2.75	12714	12.71	2.86	4.52	1.02	
22	0.559	18	0.018	16	0.016	3.10E-08	2.14E-04	505.92	3	5.83	66090	198.27	44.57	10.43	2.34	
24	0.610	18	0.018	16	0.016	3.10E-08	2.14E-04	425.12	3	6.93	50904	152.71	34.33	11.37	2.56	
24	0.610	18	0.018	16	0.016	3.10E-08	2.14E-04	425.12	2	6.93	50902	101.80	22.89	11.37	2.56	
24	0.610	18	0.018	16	0.016	3.10E-08	2.14E-04	425.12	1	6.93	50893	50.89	11.44	11.37	2.56	
22	0.559	11	0.011	9	0.009	6.35E-09	1.26E-04	298.57	3	3.43	13538	40.61	9.13	6.13	1.38	
24	0.610	11	0.011	9	0.009	6.35E-09	1.26E-04	250.88	3	4.08	10427	31.28	7.03	6.69	1.50	
24	0.610	11	0.011	9	0.009	6.35E-09	1.26E-04	250.88	2	4.08	10425	20.85	4.69	6.69	1.50	
24	0.610	11	0.011	9	0.009	6.35E-09	1.26E-04	250.88	1	4.08	10420	10.42	2.34	6.69	1.50	

* The motor can produce 10,000 rpm = 1047.2 rad/s.

*Omega is measured in rad/s.
*Delta is measured in mm.

Figure C-1 Continued

Sting



60

Figure D-1: Autocad Drawing of Sting

Assembly Drawing of Model Components

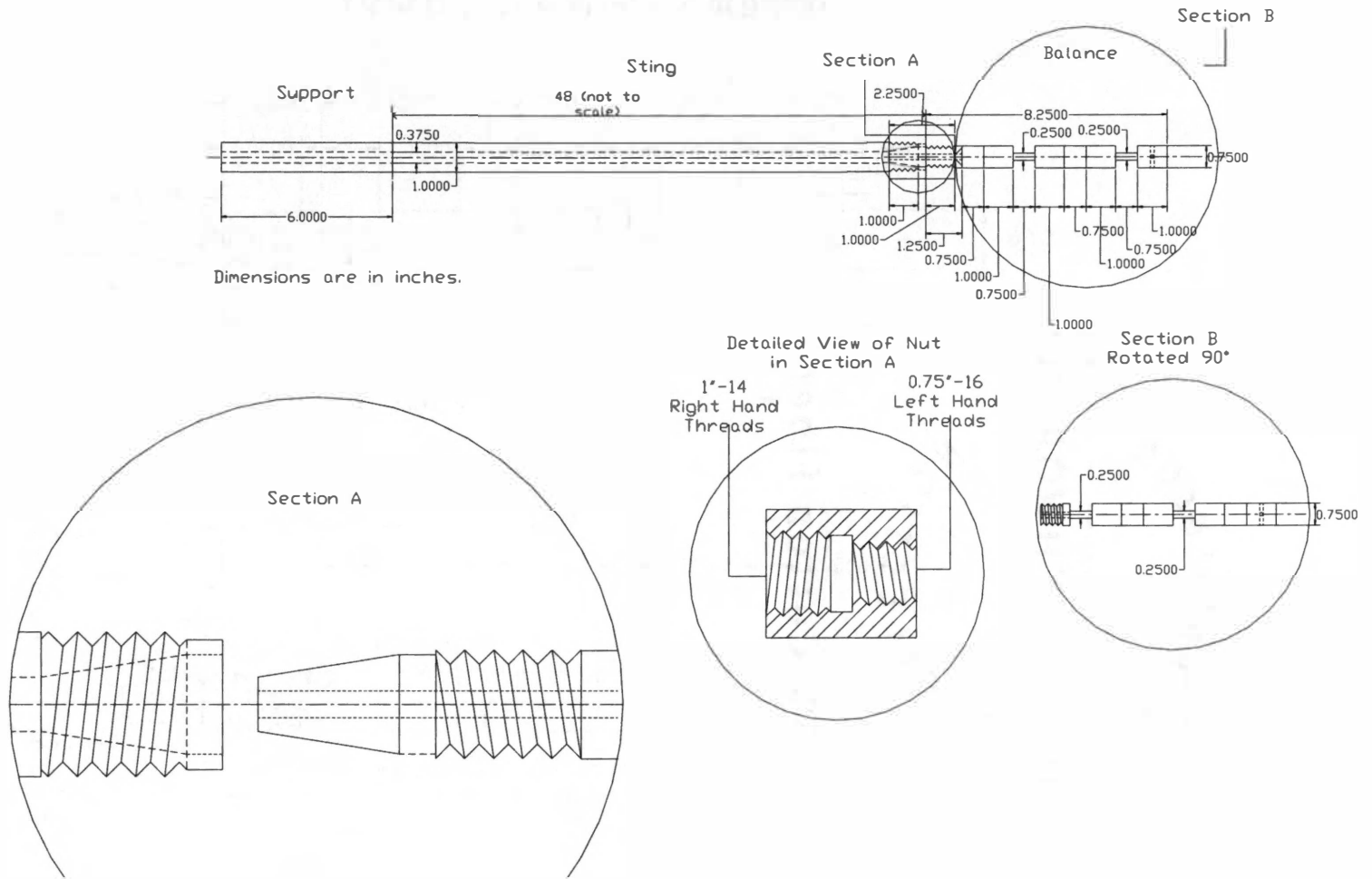


Figure D-3: Assembly Drawing of Model Components

Appendix E

Table E-1: Results Comparison For Sting Only Configuration – Tetrahedron Mesh

	Computational Results - Constrained Condition	Experimental Results - Constrained Condition	Computational Results - Unconstrained Condition	Experimental Results - Unconstrained Condition
A1	13.027	11.025		
A2	13.027			
B1	81.493	70.989	82.664	66.25
B2	81.497		82.67	
C2	227.56		227.35	182.5
C2	227.58		227.36	
D1	444.22		444.21	355.625
D2	444.25		444.24	
E	636.44			
F1	730.77		731.09	586.25
F2	730.82		731.14	
G	1027.2			
H1	1085.3		1086.3	870
H2	1085.3			
I	1505.6			

* Units are in Hertz.

Table E-2: Results Comparison For Sting Only Configuration – Quadrilateral Mesh

	Computational Results - Constrained Condition	Experimental Results - Constrained Condition	Computational Results - Unconstrained Condition	Experimental Results - Unconstrained Condition
A1	12.757	11.025		
A2	12.757			
B1	79.807	70.989	80.955	66.25
B2	79.807		80.955	
C2	222.87		222.66	182.5
C2	222.87		222.66	
D1	435.11		435.08	355.625
D2	435.11		435.08	
E	636.67			
F1	715.85		716.14	586.25
F2	715.85		716.14	
G	1027.2			
H1	1063.3		1064.2	870
H2	1063.3			
I	1475.3			

* Units are in Hertz.

Table E-3: Results Comparison for Sting + Nut Configuration

	Computational Results - Constrained Condition	Experimental Results - Constrained Condition	Computational Results - Unconstrained Condition	Experimental Results - Unconstrained Condition
A1	11.202	9.669		
A2	11.203			
B1	72.02	65.612	73.045	59.375
B2	72.022		73.046	
C2	204.52		204.48	165.625
C2	204.52		204.49	
D1	403.99		404.27	326.25
D2	404		404.28	
E	535.55			
F1	669.89		670.67	540.625
F2	669.9		670.67	
G	952.27			
H1	1000.1		1001.7	806.875
H2	1000.1			
I	1392			

* Units are in Hertz.

VITA

Kristi D. Holland was born and raised in Jackson, Mississippi. Upon graduating high school in 1998, she attended Mississippi State University in Starkville, MS where she received a Bachelor of Science Degree in Biological Engineering, with emphasis in Biomedical Engineering. She immediately began work on a Master of Science Degree in Mechanical Engineering at the University of Tennessee Space Institute in Tullahoma, TN and was awarded her degree in December 2003.